Cell

Proteome-scale movements and compartment connectivity during the eukaryotic cell cycle

Graphical abstract

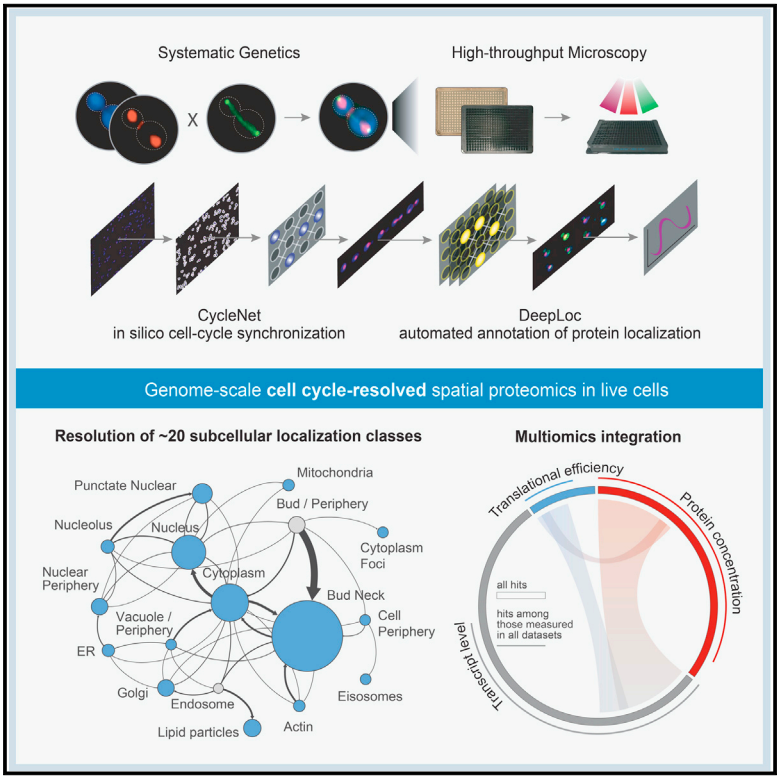

Highlights

- Genome-scale high-resolution spatiotemporal map of the yeast cell cycle proteome
- Combination of CNNs for temporal and spatial dissection of static images of live cells
- Cell cycle-resolved phenomics guides functional analysis of uncharacterized genes
- Web-based tool for data access searchable via names of yeast genes or human orthologs

Authors

Athanasios Litsios, Benjamin T. Grys, Oren Z. Kraus, ..., L. Stirling Churchman, Charles Boone, Brenda J. Andrews

Correspondence

charlie.boone@utoronto.ca (C.B.), brenda.andrews@utoronto.ca (B.J.A.)

In brief

A high-resolution spatial map of proteome dynamics during the eukaryotic cell cycle was generated via application of two distinct convolutional neural networks on images of millions of live cells. Multi-omics integration provides a comprehensive view of genome-scale molecular fluctuations associated with the eukaryotic cell cycle.

Litsios et al., 2024, Cell *187*, 1490–1507
March 14, 2024
https://doi.org/10.1016/j.cell.2024.02.014

CellPress

CellPress
OPEN ACCESS

Cell

Resource

Proteome-scale movements and compartment connectivity during the eukaryotic cell cycle

Athanasios Litsios,[1,9] Benjamin T. Grys,[1,2,9] Oren Z. Kraus,[1,3,9] Helena Friesen,[1] Catherine Ross,[1,2] Myra Paz David Masinas,[1] Duncan T. Forster,[1,2] Mary T. Couvillion,[4] Stefanie Timmermann,[5] Maximilian Billmann,[6,7] Chad Myers,[6] Nils Johnsson,[5] L. Stirling Churchman,[4] Charles Boone,[1,2,8,*] and Brenda J. Andrews[1,2,10,*]

[1]Donnelly Centre for Cellular and Biomolecular Research, University of Toronto, Toronto, ON M5S 3E1, Canada
[2]Department of Molecular Genetics, University of Toronto, Toronto, ON M5S 1A8, Canada
[3]Department of Electrical and Computer Engineering, University of Toronto, Toronto, ON M5S 3G4, Canada
[4]Department of Genetics, Harvard Medical School, Boston, MA 02115, USA
[5]Institute of Molecular Genetics and Cell Biology, Department of Biology, Ulm University, Ulm 89081, Germany
[6]Department of Computer Science and Engineering, University of Minnesota, Minneapolis, MN 55455, USA
[7]Institute of Human Genetics, University of Bonn, School of Medicine and University Hospital Bonn, Bonn, Germany
[8]RIKEN Center for Sustainable Resource Science, Wako 351-0198 Saitama, Japan
[9]These authors contributed equally
[10]Lead contact
*Correspondence: charlie.boone@utoronto.ca (C.B.), brenda.andrews@utoronto.ca (B.J.A.)
https://doi.org/10.1016/j.cell.2024.02.014

SUMMARY

Cell cycle progression relies on coordinated changes in the composition and subcellular localization of the proteome. By applying two distinct convolutional neural networks on images of millions of live yeast cells, we resolved proteome-level dynamics in both concentration and localization during the cell cycle, with resolution of ~20 subcellular localization classes. We show that a quarter of the proteome displays cell cycle periodicity, with proteins tending to be controlled either at the level of localization or concentration, but not both. Distinct levels of protein regulation are preferentially utilized for different aspects of the cell cycle, with changes in protein concentration being mostly involved in cell cycle control and changes in protein localization in the biophysical implementation of the cell cycle program. We present a resource for exploring global proteome dynamics during the cell cycle, which will aid in understanding a fundamental biological process at a systems level.

INTRODUCTION

The eukaryotic cell cycle is a series of molecular events leading to accurate genome duplication and cell division. Abnormal execution of the cell cycle program can detrimentally impact cellular and organismal fitness and is a hallmark of disease.[1,2] Key cell cycle regulators are highly conserved, and cell cycle progression features periodic activation and repression of cyclin-dependent kinases (Cdks), transcription factors, and components of the proteolytic machinery, among other regulators.[3] The central biological importance of the cell cycle, together with its widespread implication in disease, has motivated efforts to systematically characterize molecular fluctuations associated with cell cycle progression. Several "omics" projects have cataloged cell cycle-dependent changes in the transcriptome, proteome abundance, phosphoproteome, and metabolome in a number of model systems, generating significant insights about cell cycle regulation.[4–20] For example, a system of coupled oscillators orchestrates the expression of ~1,300 genes during the yeast cell cycle,[7] and a large fraction of the proteome exhibits periodic abundance, with metabolic activity also fluctuating to support cell cycle-specific proteosynthetic requirements.[18]

However, despite subcellular compartmentalization being a distinctive feature of eukaryotic cells, our understanding of the spatial distribution of the proteome during the cell cycle remains relatively limited, generally due to technical challenges associated with large-scale measurements of the subcellular localization of proteins, particularly in living cells. Early efforts made use of time-lapse images of human lung cancer cells expressing 495 proteins tagged with yellow fluorescent protein (YFP) at an internal exon, to show that cell cycle-dependent localization changes may be more prevalent than alterations in protein levels.[21] More recently, spatial dynamics of the proteome during the cell cycle were assessed on a larger scale by mining the Cell Atlas within the Human Protein Atlas, a collection of images of fixed cells from asynchronous cell lines stained with validated

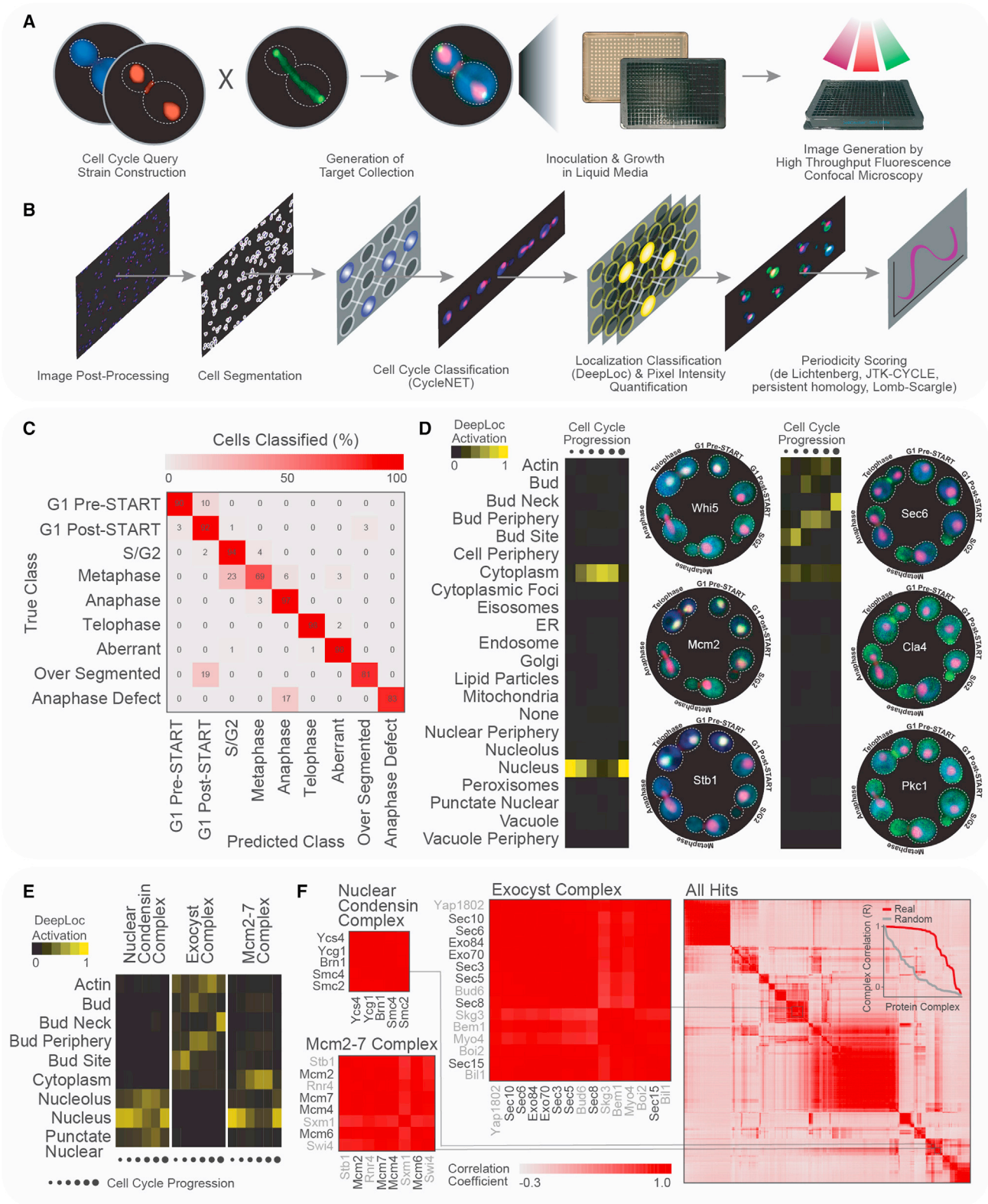

(legend on next page)

antibodies.[22] In this study, 230 proteins localizing to mitotic structures were identified, approximately half of which had not been previously shown to be associated with the cell cycle. Nevertheless, we still lack a detailed, cell cycle-resolved view of proteome localization changes in any eukaryotic cell.

Here, we mapped with high resolution the spatiotemporal dynamics of the budding yeast proteome as a function of cell cycle progression, using high-content imaging of live cells. To achieve this, we combined high-throughput fluorescence microscopy of cells expressing GFP-fusion proteins with neural networks for automated cell cycle-stage classification and annotation of proteins to 22 subcellular location classes. We show that a quarter of the assessed yeast proteome displays cell cycle-related periodicity, with proteins tending to be periodic either in localization or concentration during the cell cycle, but most often not in both. Individual cell cycle transitions are characterized by unique spatiotemporal proteome signatures, with proteins with periodic concentration being primarily involved in cell cycle control, whereas those with periodic localization in the biophysical implementation of the cell cycle program. Complementation of our single-cell proteome measurements with cell cycle-resolved transcriptome and ribosome profiling data, suggests an important role of post-translational regulation in determining cell cycle-specific protein concentrations. Finally, we integrated our spatial information with the dynamic proteome concentration data to generate quantitative protein flux maps and demonstrate how cell cycle-resolved phenomics can guide functional genome annotation. Our study provides a comprehensive view of proteome dynamics with high spatial resolution, offering a unique resource for exploring molecular fluctuations associated with the eukaryotic cell cycle. All data can be accessed at thecellvision.org/cellcycle.

RESULTS AND DISCUSSION

A high-content screening pipeline for quantification of spatiotemporal proteome dynamics in living cells

To explore the yeast proteome for cell cycle-specific changes in protein localization and concentration, we implemented a single-cell imaging pipeline that exploits the yeast protein-GFP collection, a resource consisting of thousands of strains expressing different proteins tagged C-terminally with GFP, at their endogenous loci.[23] The GFP collection contains 4,100 strains (of a possible ~5,800) that have a GFP signal above background in standard growth conditions,[24–26] enabling visualization of ~75% of the yeast proteome. The GFP collection has been extensively used and validated by comparison to other data, such as mass-spectrometric measures of protein abundance,[27] and available literature about individual protein localizations.[25] The first step in our imaging pipeline involves using the synthetic genetic array (SGA) method[28] to introduce additional fluorescent markers into the arrayed GFP collection to enable automated cell segmentation of images (Figure 1A). Specifically, we introduced three red and far-red fluorescent proteins into every strain in the GFP collection, marking the cytoplasm of the cell, the nucleus, and the bud neck (Figure 1A). We performed SGA in biological triplicate, after which we imaged our arrays using a high-throughput (HTP) spinning-disc confocal microscope. We generated >123,000 images of more than 20 million live cells from an asynchronous cell population and identified single cells in our images using a computational cell segmentation algorithm (STAR Methods; Figure 1B).

To extract cell cycle-specific information from segmented cells, we developed a supervised neural network, which we call CycleNET, to perform *in silico* cell cycle synchrony (Figure 1B). CycleNET learns feature information directly from the single-cell images and relies on the fluorescent markers of the cytoplasm, nucleus, and bud neck in our arrays to determine cell cycle position. Based on the dynamics of these structures, we developed a cell cycle classification framework for binning single-cell images into one of six cell cycle stages: G1 Pre-START, G1 Post-START, S/G2, metaphase, anaphase, and telophase (Figures S1A–S1C; STAR Methods). To ensure reliable cell cycle classification, we incorporated additional output classes to filter dead cells, non-cellular objects, improperly segmented cells, and cells with anaphase defects. We labeled 12,717 single cells and used 90% of the data to train CycleNet and the remaining 10% to evaluate the model's classification performance. This led to a classifier that performed with >93% accuracy when tested against a separate subset of manually annotated single-cell images (Figure 1C). Thus, CycleNET can be used for reliable cell cycle classification of single cells from asynchronous cell populations. In addition, due to the *in silico* nature of the synchronization, cell cycle-specific proteome data quantified via CycleNET are devoid of common issues caused by continuous live cell fluorescent imaging such as fluorophore bleaching.

To extract dynamic protein localization information from the cell cycle-classified cells, we combined CycleNet with DeepLoc (Figure 1B). DeepLoc is a neural network we previously developed that enables automated identification of subcellular

Figure 1. A high-content screening pipeline for quantification of spatiotemporal proteome dynamics in living cells

(A and B) Overview of our automated image (A) generation and (B) analysis pipelines.

(C) Error matrix for the performance of CycleNET when tested against manually labeled single-cell images. The percentage of cells classified for each class comparison is shown.

(D) Clustergram cross-sections showing the average cell cycle localization vector (DeepLoc activation) for example proteins that are known to move between the nucleus and cytoplasm (n = 10; left), or to regions of polarized growth (n = 36; right) during cell cycle progression (x axis). Example micrographs for three proteins in each case are shown (cytoplasm displayed in blue, the nucleus and septin in red/pink, and the protein of interest in green).

(E) Same as in (D) for members of the indicated protein complexes.

(F) Clustergram showing the pairwise correlation of all localization hits after hierarchical clustering. Inset shows the mean correlation of proteins annotated to the same complex (real, red line) versus the mean correlation of random proteins of the same size as a given complex (random, gray line). Correlations between members of specific protein complexes (exocyst, condensin, and Mcm2-7 complex) are highlighted. Dark gene names denote members of the respective complex; two members of the MCM complex were not included in the GFP collection.

See also Figure S1.

protein localization.[24] Specifically, following cell cycle classification, single-cell images were processed through DeepLoc to quantify the localization of GFP-fusion proteins in 22 unique subcellular localization classes. This operation produced a vector of information for each protein of interest, enabling quantitative measures of localization through the cell cycle; mean GFP pixel intensity for each segmented cell in the image was also extracted, as a proxy for protein levels (see below). To evaluate the performance of DeepLoc in our dataset, we tested it against a separate subset of manually annotated single-cell images. Here, DeepLoc performed in the cell cycle-classified dataset with 83.7% accuracy, with misclassification occurring only between related localization classes like the vacuole with vacuole periphery and bud with bud periphery (Figure S1D).

Proteome-scale identification of cell cycle-specific localization changes

To identify proteins that display dynamic localization during the cell cycle, we implemented strict statistical scoring metrics previously used for analyzing periodicity in gene expression data,[12,29] namely: de Lichtenberg, JTK_CYCLE, persistent homology, and Lomb-Scargle.[30–34] We identified a high-confidence list of 405 proteins whose localization changes during the cell cycle (Table S1). The list includes proteins known to display cell cycle-specific localization changes, such as the G1 transcription repressors Whi5 and Stb1,[35] and proteins involved in polarized cell growth, such as the Cla4[36] and Pkc1[37] kinases (Figure 1D). We also detected a number of protein complexes known to span a range of different localization classes, including the mini-chromosome maintenance (MCM) complex, which includes Mcm2 (Figure 1D), that shuttles to the cytoplasm during G1/S phases and returns to the nucleus during cytokinesis[38–40] (Figure 1E); the Exocyst Complex, which includes Sec6 (Figure 1D), that moves from the bud site in G1, to the bud periphery during S/G2 and early mitosis, and to the bud neck at the onset of cytokinesis[41–44] (Figure 1E); and the nuclear condensin complex, which shows more subtle intranuclear movements[45] (Figure 1E). Clustering of the pairwise localization profiles for all hits revealed high correlation between individual protein complex components (Figure 1F). This correlation among protein complex members extended beyond these three examples and constituted a general feature of our dataset (Figure 1F, inset). Finally, we used t-distributed stochastic neighbor embedding (t-SNE) to visualize all our cell cycle-resolved localization data (Figure S1E). Post-annotation of the plotted data based on a manually curated functional standard revealed co-clustering of proteins involved in similar bioprocesses despite the input being solely localization information (Figure S1E), indicating that the quantitative analysis of the yeast protein-GFP localization data is rich in functional information.

In addition to detecting previously known changes in protein localization, our list also includes many proteins that had not been previously reported to display cell cycle-specific localization, providing a resource for future analyses. For example, Cks1, the phosphoadaptor of the master cell cycle kinase Cdk1,[46] was both nuclear and cytoplasmic throughout the cell cycle, consistent with previous reports,[23] but its relative distribution changed such that it was primarily nuclear following cell cycle START, until cytokinesis when its cytoplasmic localization increased until the next round of cell division (Figure S2A). The similar dynamic localization profiles of Cdk1[47] and Cks1 (Figure S2A) are consistent with Cks1 functioning as a regulatory subunit in a Cdk1-Cks1 complex. Although the localization of Cks1 to both the nucleus and cytoplasm is obvious from visual inspection of the microscopy images, our unbiased computational analysis also identified cell cycle-specific changes in localization that were challenging to detect manually.

Cell cycle-specific changes in protein localization included compartments not typically associated with cell cycle regulation, such as the Golgi. In particular, we observed a subtle periodic localization change of both the actin-interacting protein Aip1 and the cyclase-associated protein Srv2 to the Golgi at the beginning and end of the cell cycle (Figure S2A). These proteins both predominantly localize with actin and physically interact with one another[48] and with cofilin, Cof1,[49] which is involved in actin filament depolymerization.[50] Although Aip1 and Srv2 do not have an established function in the Golgi, Cof1 is involved in the selective sorting and export of secretory cargo from the late Golgi.[51] Together with our data, these observations suggest that Aip1 and Srv2 may facilitate Cof1's function at the Golgi in a cell cycle-dependent manner with regulation taking place at the level of protein localization. We also observed a subtle periodic movement of the chitin synthase-related protein Chs7, which is involved in regulating Chs3 export from the endoplasmic reticulum (ER) to the bud neck where it is required for synthesis of the chitin ring during bud emergence.[52,53] Our analysis annotated Chs7 primarily to the bud neck and vacuole, consistent with previous work[23]; however, we also detected a subtle periodic movement of Chs7 to the ER during G1 (Figure S2A). The timing of this localization change coincides with Chs3 export prior to bud emergence, suggesting that the cell cycle-specific regulation of this process might be occurring at the level of Chs7 localization.

The landscape of proteome movements and compartment connectivity during the cell cycle

To gain a global overview of proteome movements during the cell cycle, we asked which cellular compartments are involved in the localization changes that we identified. The compartment featuring the most cases of change in protein localization was the cytoplasm (Figure 2A), consistent with the primarily cytosolic localization of many proteins (~37%) and the physical connection between the cytoplasm and other compartments (Figure S2B). Many localization changes also involved compartments associated with the bud and its formation, and the nucleus, with localization changes involving these classes being the most pronounced in terms of magnitude (Figure 2A). Overall, protein movements involving the cytoplasm and the bud- and nucleus-related localization classes comprised nearly three-quarters of the cell cycle-dependent protein localization changes that we detected (Figure 2A, inset). Notably, we found very few localization changes involving the mitochondria, despite a substantial fraction of the studied proteome (~12%) residing in this compartment (Figures 2A and S2B), indicating that any cell cycle-dependent aspects of mitochondrial function are unlikely to be regulated by protein localization changes.

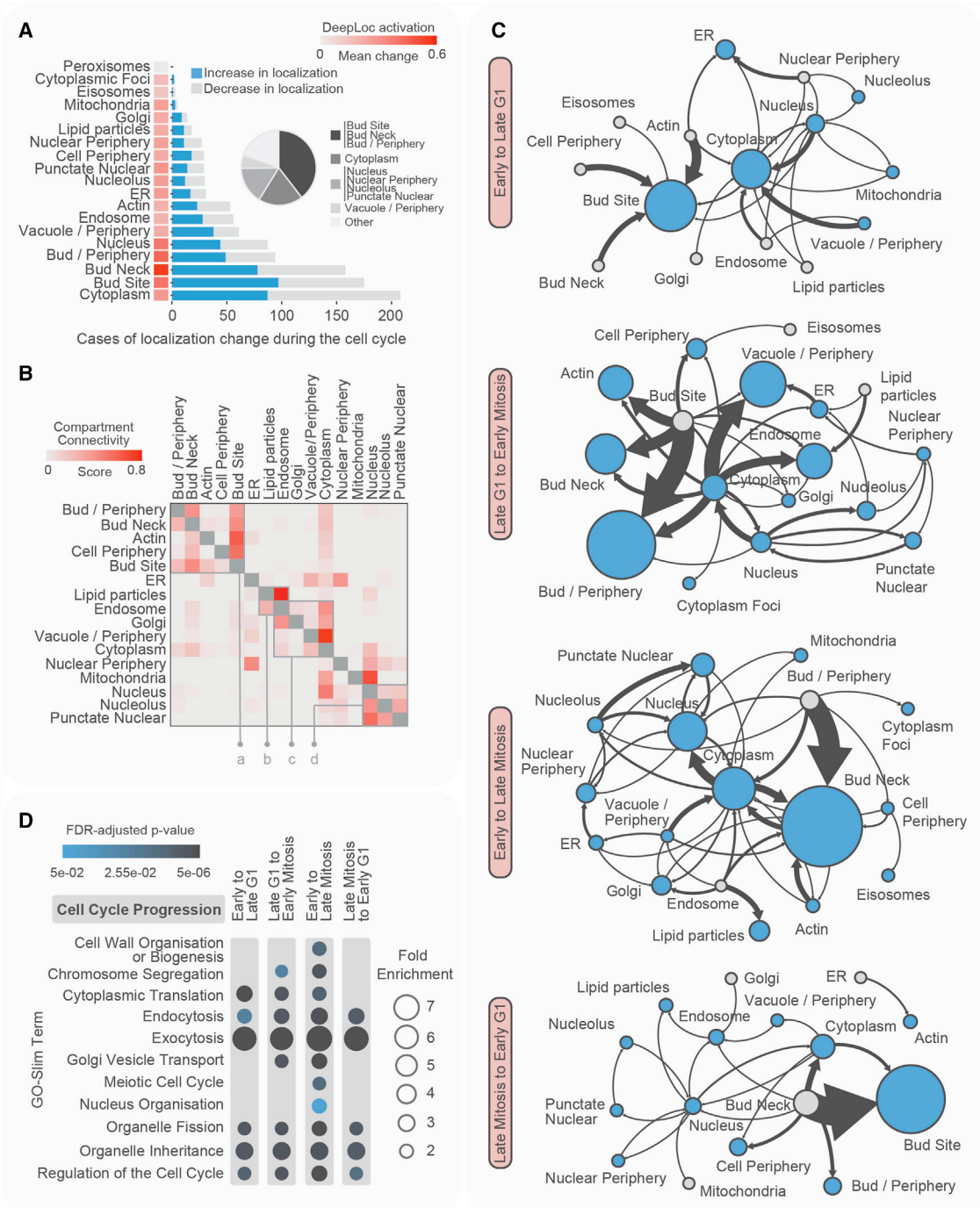

Figure 2. The landscape of proteome movements and compartment connectivity during the cell cycle

(A) Number of cases of localization changes and their mean magnitude per localization class during the cell cycle (mean change in DeepLoc activation; red bars). Inset: fraction of all identified cases of protein movement involving the indicated localization classes.

(B) Connectivity of different localization classes in terms of protein movements within them. The four boxed regions marked a, b, c, and d are analyzed further in Figure S2D.

(C) Map of protein movements during each major cell cycle transition. Each node represents a different localization class. The size of the blue nodes reflects the total number of proteins whose localization increases at the specific class. Gray nodes represent classes for which there is no increase in protein localization. Arrow thickness reflects the number of unique proteins moving from one localization class to another.

(D) Functional enrichments (Gene Ontology [GO]-Slim terms) of proteins moving at each cell cycle transition.

See also Figure S2.

To understand which localization classes exchange proteins during the cell cycle, we calculated a compartment connectivity score (STAR Methods) (Figure 2B) and assessed the direction and magnitude of protein movements. Highly connected compartments included the bud-related localization classes, the cytosol and the bud neck, the nucleus, and the vacuole, as well as the nucleus-related classes (Figures 2B and S2C). Proteins moving within the nucleus, nucleolus, and punctate nuclear classes, were significantly enriched for genes functionally annotated with chromosome segregation and DNA replication roles, suggesting that these processes may be regulated at the level of intra-compartmental protein movements (Figure S2D).

Major localization classes, such as the cytoplasm and the nucleus, were involved in constant bidirectional protein movement, with proteins moving in and out of them for the whole duration of the cell cycle (Figure S2E). However, movements involving some other localization classes, such as the vacuole and the endosome, tended to be confined to specific cell cycle transitions, as were movements for localization classes with a cell cycle-specific presence, such as the bud site and the bud (Figure S2E). Overall, we found that each major cell cycle transition was dominated by movements of proteins to particular localization classes (Figure 2C). Specifically, G1 progression was characterized by movement of proteins from the cell periphery and actin toward the bud site, as well as from the nucleus to the cytoplasm. After commitment to the cell cycle and onset of mitosis, proteins that were previously localized to the bud site became part of the bud neck or were distributed to the bud periphery and actin. Movement of proteins from the cytoplasm to the vacuole or its periphery was also observed during late G1 to early mitosis. During mitotic progression, and specifically at telophase, proteins localized previously at the bud and its periphery accumulated at the bud neck. In parallel, there was protein exchange between the cytosol and the bud neck, and we also observed substantial intranuclear movement. The reset of the cell cycle from the end of mitosis and the entry to G1 were marked by the movement of proteins from bud neck to the incipient bud site, or to the cytosol. Thus, cell cycle transitions are associated with coordinated movements of proteins toward cell locations involved in major physical events of the cell cycle, such as daughter cell formation, chromosome segregation, and cytokinesis.

Consistent with these observations, we found significant functional enrichments among dynamic proteins associated with all major cell cycle transitions (Figure 2D). The subset of proteins moving during mitosis was enriched for proteins involved in chromosome segregation, nucleus organization, and cell wall organization or biogenesis, consistent with the mitotic events and dramatic changes in cell size and geometry associated with this cell cycle stage. However, proteins with annotated roles in bioprocesses related to the logistical implementation of the cell cycle program, such as organelle fission and inheritance, endocytosis and exocytosis, were enriched across all cell cycle stages. We also observed enrichment for proteins involved in cytoplasmic translation in all cell cycle transitions except for telophase to early G1, consistent with cell cycle-dependent regulation of protein synthesis throughout much of the cell cycle (explored further below).

In summary, we describe a set of 405 proteins that exhibit significant changes in localization during the cell cycle, involving movements between nearly 20 distinct subcellular localizations. These localization dynamics together with the image dataset and a cell cycle viewer are available at TheCellVision.org[54] (thecellvision.org/cellcycle). Many key cell cycle regulators and their associated regulatory pathways are highly conserved, with many genes first characterized in yeast performing similar roles in human cells. To facilitate the use of our resource to explore human cell cycle biology, the results section for each yeast gene on TheCellVision.org includes information about the respective human ortholog(s), and the website is also directly searchable using human gene names.

Global proteome content is dynamic during the cell cycle

To acquire a comprehensive view of proteome dynamics during the cell cycle, we complemented our cell cycle-specific localization data with quantitative protein concentration measurements. Specifically, we used the same segmented cells from which we extracted the cell cycle-resolved protein movements, to calculate the mean GFP pixel intensity as a proxy for protein concentrations. Our protein abundance measurements correlated well with previous estimates of protein abundance from images of the protein-GFP collection[25] (Figure S3A), flow cytometry analysis of the same collection[55] (Figure S3B), and peptide abundance data generated by mass spectrometry[18] (Figure S3C). In fact, our GFP-based protein abundance measurements correlated as well with abundance measurements based on label-free mass-spectrometry approaches, as independent mass-spectrometry datasets correlated with each other[27] (Figure S3D), suggesting that the GFP tag does not cause systematic effects on protein stability. Moreover, cyclins peaked in abundance at the expected cell cycle phases (Figure S3E), indicating that GFP maturation (half-time ~17–27 min)[56,57] was not limiting for identifying cell cycle-specific changes in protein concentration in our conditions (doubling time ~3 h).

We first examined our data for changes in total proteome content, which we found to be cell cycle-dependent. Specifically, protein concentration globally increased during G1, peaking at late G1 and decreasing after commitment to the cell cycle (Figure 3A). This finding was unexpected since protein abundances tend to be proportional to cell size[58] and differential scaling between protein abundance and cell size during G1 has only been observed for a handful of proteins.[59,60] To confirm our observations, we analyzed orthogonal measurements of the cell cycle-resolved proteome generated using mass spectrometry.[18] Consistent with our findings, the total number of protein molecules per dry cell weight peaks in G1 and decreases later in the cell cycle (Figure S3F).

To further explore the increase in proteome concentration during G1, we examined the dynamics of individual proteins. We focused on proteins with GFP fluorescence at least 5% higher than background cellular autofluorescence across all relevant cell cycle phases and biological replicates (n = 2,853; see STAR Methods). We found that 2/3 of the proteins (n = 1,946) increased in concentration during G1, and thus, their abundance displayed a positive differential scaling with cell size (Figure 3B

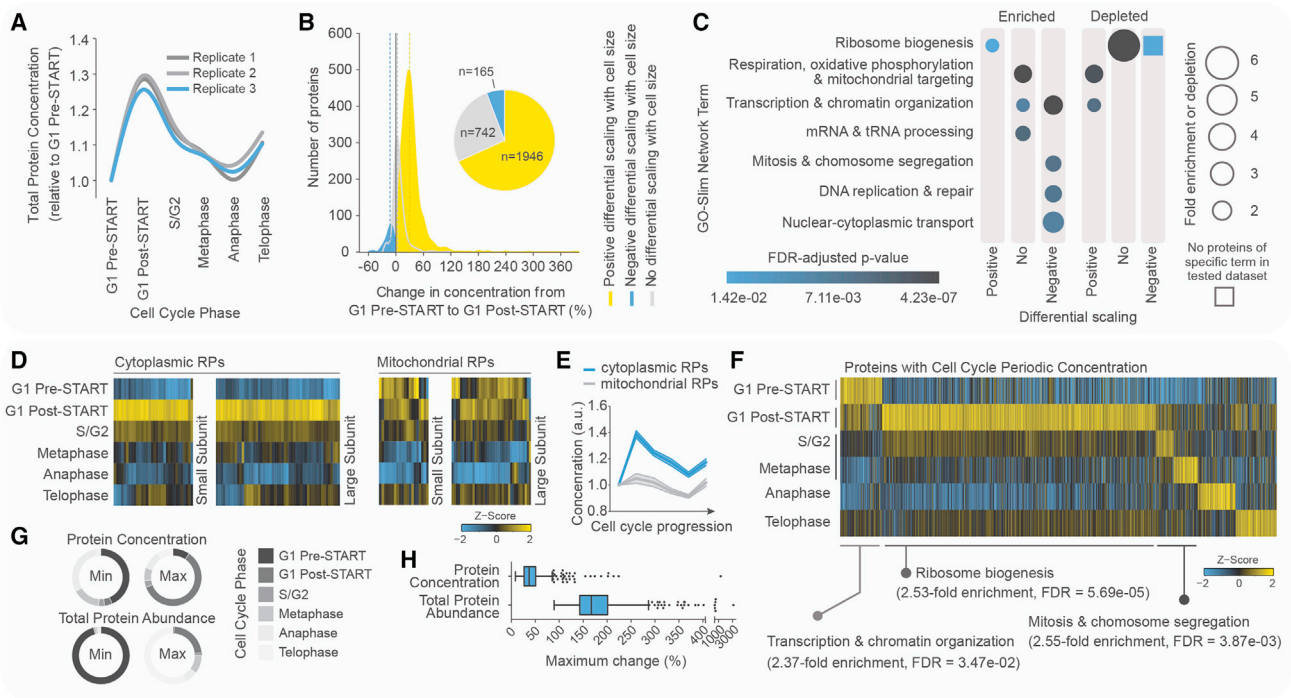

Figure 3. Proteome concentration dynamics during the cell cycle

(A) Change in sum concentration (mean autofluorescence-corrected GFP) of all proteins relative to G1 Pre-START (n = 3,806; ~70% of total proteome content). The smoothing spline for each replicate measurement is graphed separately.

(B) Percent change in concentration from G1 Pre-START to G1 Post-START for the 2,853 proteins with GFP fluorescence of ≥5% than background. Proteins are grouped according to the scaling of their abundance with cell size. Vertical dashed lines denote the median change in each group. Inset: fraction of proteins showing positive, negative, and no differential scaling with cell size during G1.

(C) Significant functional enrichments or depletions (GO-Slim network terms) for protein groups in Figure 3B. Functional analyses for more detailed bioprocess terms are presented in Table S2.

(D) Heatmaps showing the concentration dynamics of cytoplasmic (n = 85) and mitochondrial (n = 58) ribosomal proteins (RPs) during the cell cycle (clustering: average linkage, Pearson).

(E) Changes in the concentration of proteins in (D) relative to G1 PreSTART (mean ± SEM [line and shading, respectively], arbitrary units as in A).

(F) Heatmap showing the concentration dynamics of proteins identified as periodic, ordered by the descending concentration at each cell cycle phase prior to *Z* score estimation. Proteins with levels above cellular autofluorescence in all indicated cell cycle phases are shown (n = 731). Functional enrichments are presented for proteins peaking at G1 Pre-START, G1 Post-START, and S/G2-metaphase.

(G) Relative fractions of proteins with periodic concentration that display their max or min concentration or abundance at each cell cycle phase.

(H) Tukey boxplots showing the maximum change (mean among three replicates) in protein concentration and total protein abundance during the cell cycle of periodic proteins (n = 545) with features permitting the confident quantitative assessment of these parameters (STAR Methods).

See also Figure S3.

inset; STAR Methods). The concentration of most of the remaining proteins (n = 742) did not exhibit a clear increase or decrease during G1, including the G1-transcription repressor Whi5 (0.6 ± 4.5% change [mean ± SEM]) whose G1 dynamics have been a matter of debate, suggesting that their abundance changes proportionally with cell size.[60–65] Finally, only ~6% of the tested proteins (n = 165) decreased in concentration during G1, exhibiting negative differential scaling of abundance with cell size. Thus, the abundance of most proteins scales differentially with cell size during G1. In addition, the median increase in concentration during G1 of proteins with positive differential scaling was ~30%, whereas the median decrease of those with negative differential scaling was only ~13% (Figure 3B). Functional analysis showed that proteins that increase in concentration during G1 are enriched for ribosome biogenesis but are depleted for proteins involved in transcription and chromatin organization (Figure 3C). By contrast, proteins whose concentration did not change or decreased during G1 were depleted for ribosome biogenesis and enriched for transcription and chromatin organization (Figure 3C). These data suggest that the observed increase in proteome concentration during G1 mainly reflects changes in translation, rather than transcription.

Although proteins that increased in concentration during G1 were enriched for annotations to cytoplasmic translation, they were depleted for mitochondrial translation, pointing toward differences between the dynamics of the cytoplasmic and mitochondrial translational machineries during the cell cycle (Table S2). Indeed, the concentration of cytoplasmic ribosomal proteins (RPs) increased during G1 and decreased thereafter, whereas the concentration of mitochondrial proteins remained fairly constant during the cell cycle (Figures 3D and 3E). Given the lack of evidence for dynamic regulation of RP stability during

the cell cycle, the decrease in concentration of cytoplasmic RPs at S/G2 and halfway through metaphase (Figure 3E) likely reflects a decrease in their production after G1 and consequent dilution due to increasing cell size. By contrast, the relatively constant concentration of mitochondrial RPs (Figure 3E) suggests that these proteins are continuously produced throughout the cell cycle. The same pattern was observed for aminoacyl-tRNA synthetases (ARSs) (Figures S3G and S3H). Recent continuous measurements of cytoplasmic RPs Rpl13a and Rpl2a in single cells suggested that their production rate increases faster than cell volume during G1, decreases after G1, and then starts to increase again late at the cell cycle,[66] consistent with the pattern we observed for the whole cytoplasmic ribosomal proteome. The same trend was observed in the synthesis rate of GFP expressed via the TEF promoter during the cell cycle in single cells.[60] Collectively, these findings point toward increased protein biosynthetic activity during G1, consistent with mass-spectrometry studies.[18]

Global changes in protein synthesis during the cell cycle are coordinated with metabolic dynamics[18,60] and glucose uptake rate increases during G1 progression.[60,67] Consistent with these observations, we found that all glycolytic enzymes in our dataset increased in concentration during G1 (median increase ~31%) (Table S2), whereas the concentration of proteins involved in respiratory metabolism tended to either remain constant or undergo more modest changes (median increase of those with positive differential scaling ~18%) (Table S2; Figure 3C). For example, hexokinases (Hxk1 and Hxk2; 32 ± 6% and 31 ± 1% [mean ± SEM], respectively) and phosphofructokinases (Pfk1 and Pfk2; 33 ± 5% and 37 ± 7% [mean ± SEM], respectively), which catalyze two out of the three irreversible steps of glycolysis, increased in concentration as did both the low- and high-affinity glucose transporters Hxt3 (31 ± 10%) and Hxt2 (50 ± 6%; mean ± SEM). Our data also confirmed the recently reported cell cycle-specific changes in the concentration of enzymes involved in ergosterol biosynthesis,[4] as nearly all related enzymes that were present in our analysis (16 out of 20) increased in concentration during G1 (Table S2). In fact, the two proteins with the largest decrease in concentration during G1 (~50%), Fat1 and Pry3, are involved in lipid transport.[68–72]

The concentration of ~800 proteins shows cell cycle periodicity independently of the global proteome trend

To identify proteins that have periodic concentration during the cell cycle, independently of the global trend in proteome content, we applied the four statistical scoring metrics we used to study periodic protein localization to our abundance measurements. We identified 810 proteins that change in concentration during the cell cycle (Table S1; Figure 3F). Our list includes well-studied cell cycle regulators that are known to change in abundance with cell cycle progression, including the mitotic inhibitor Sic1, which peaks in G1,[73] the S-phase transcription factor Hcm1 peaking in S/G2,[74] the B-cyclin Clb2 and the Polo-like kinase Cdc5 peaking in early mitosis,[75,76] and the mating-type regulator Ash1 peaking toward the end of the cell cycle[77] (Figure S3I). We compared our data to the results from other studies that examined cell cycle-specific protein concentration dynamics using different synchronization and quantification approaches (Figure S3J). Here, despite the different approaches, we observed ~40% and ~70% agreement with the studies that used mass spectrometry to measure protein concentrations in extracts from cells synchronized by treatment with alpha factor,[18,20] validating our imaging-based approach for detecting cell cycle-specific changes in protein concentration. We observed less agreement (~9%) with mass-spectrometry-based measurements of protein abundance after synchronization using elutriation,[4] which may reflect the different metrics and statistical thresholds used for scoring periodicity, consistent with the relatively low inter-study agreement seen even when similar synchronization and quantification approaches were used (Figure S3J).

From the 810 proteins that we identified as periodic in concentration, ~60% of them peaked at late G1, <10% peaked in early G1, <4% in S/G2, and the rest were spread almost evenly among the different sub-phases of mitosis (Figures 3F and 3G). Proteins peaking at different cell cycle phases showed biologically sensible bioprocess enrichment. Specifically, proteins peaking in concentration in early G1 were enriched for genes annotated to transcription and chromatin organization functions (Figure 3F), consistent with our observation that these proteins tend to decrease in concentration as cells progress further through G1 (Figure 3C). Proteins peaking at late G1 were enriched for ribosome biogenesis (Figure 3F), again consistent with our analysis of the global proteome as cells progress through G1 (Figure 3C), and the high demands for protein synthesis as cells increase in size and commit to the cell division cycle.[60] Finally, proteins peaking at S/G2 and metaphase were enriched for mitosis and chromosome segregation.

The median maximum change in the concentration of periodic proteins in our data was ~40% (Figure 3H), in excellent agreement with recent mass-spectrometric measurements.[18] However, the maximum change in the total abundance of each protein was substantially more pronounced (~170%) (Figure 3H), consistent with changes in protein abundance during the cell cycle being largely buffered by changes in cell size, such that protein concentrations are less variable. Due to this phenomenon, most periodic proteins displayed their maximum concentration in late G1 as described earlier, despite their higher abundance in terms of absolute copy number toward the end of the cell cycle when cells are the largest (Figure 3G).

Multi-level regulation of cell cycle-specific protein concentration dynamics

To understand how periodicity in protein concentration emerges during the cell cycle, we generated cell cycle-specific transcript and translation datasets. Our main goal was to facilitate a comparison of cell cycle transcript, translation, and proteome levels, from measurements produced using the same strain background and analyzed using the same scoring metrics. Briefly, we synchronized cells in G1 phase with alpha factor, and isolated cells at five time-points after release into fresh medium, corresponding to the phases used for *in silico* synchrony of our proteomics data (G1 Post-Start; S/G2; metaphase; anaphase and telophase; G1 Pre-Start was excluded due to the method of synchrony). We performed RNA sequencing and ribosome profiling on the same samples in biological duplicate and scored these data for periodicity using the same computational scoring pipeline we applied to our proteomics datasets. Our cell cycle-resolved replicates

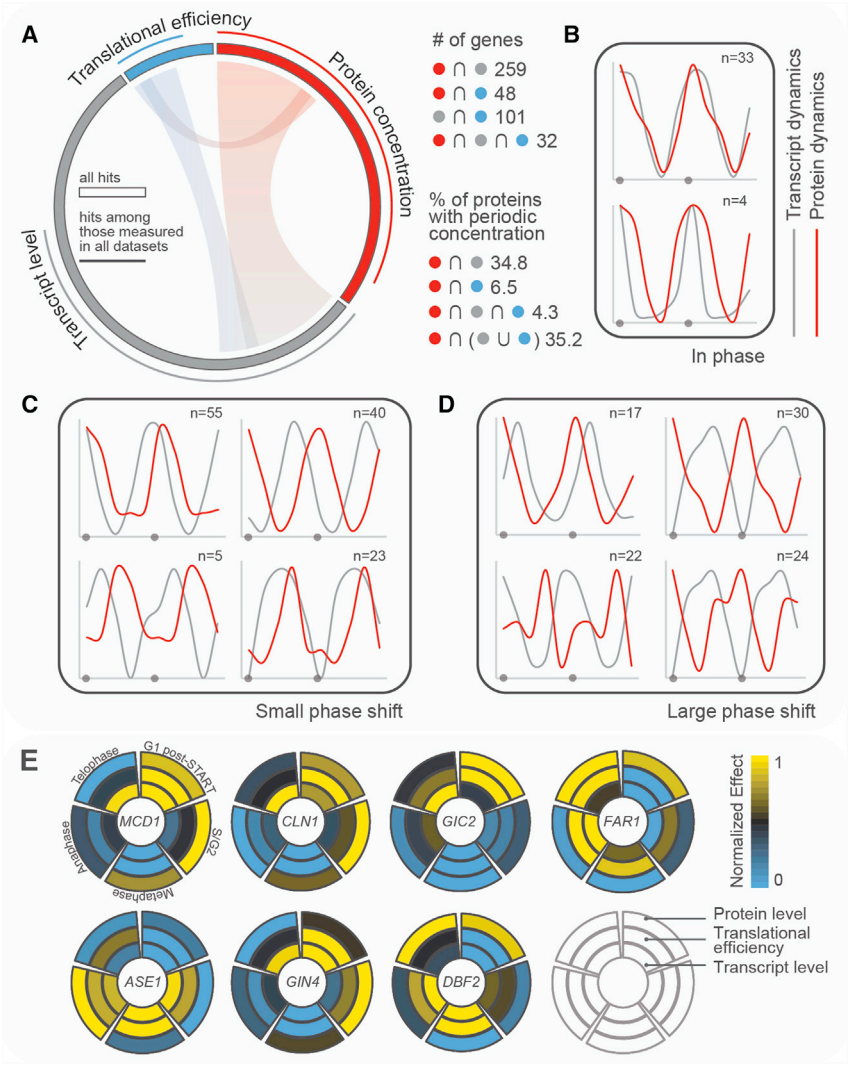

Figure 4. Multi-level regulation of cell cycle-specific protein concentration dynamics

(A) Circos[81] plot illustrating the fraction of common hits among the protein concentration (red), transcript level (gray), and translational efficiency (blue) datasets. The size of each ideogram represents the number of hits in each dataset. For example, since there are 810 protein concentration hits and 213 translational efficiency hits, the red ideogram is ~3.8 times larger than the blue ideogram. The number of common hits between datasets is summarized, along with the percentage of protein concentration hits that are also hits in other datasets (percentage calculated based on common genes measured in all datasets). ∪ = *or*, ∩ = *and*.

(B–D) Line graphs showing the averaged, normalized transcript level and protein concentration for genes with similar coordination between the two. The x axis denotes cell cycle progression, and the gray circles indicate G1. For illustration purposes, the same averaged signal for each group is presented twice (from G1 Post-START through telophase) to visually reflect the dynamics across two consecutive cycles.

(E) Selected cell cycle-specific profiles showing normalized transcript level, translational efficiency, and protein concentration dynamics for genes that were identified to be periodic in all three.

See also Figure S4.

within each experiment, for both the transcript level and translational efficiency measurements, correlated well with each other (Figures S4A and S4B), and when we combined all our single-cell and population-level measurements, they reproduced the previously reported tri-level relationship between protein concentration, transcript level, and translational efficiency measurements[4,18,78] (Figure S4C).

We identified 1,367 transcripts with cell cycle-related periodicity of which 1,255 had periodic concentration (Table S3), 213 had periodic translational efficiency (Table S3), and 101 both. Our list of cell cycle-periodic transcripts was in good agreement with other studies, which have spanned decades[4,7,12,18,74,79,80] (Figure S4D). Transcripts with periodic concentration were enriched for cell cycle-specific gene ontologies (Table S3), whereas transcripts with periodic translational efficiency were not significantly enriched for any specific bioprocess, but included genes involved in cell cycle-related processes (Table S3).

Although we saw high correlation between overall transcript and protein levels in our data (Figure S4C), only a fraction of all proteins with periodic concentration were encoded by genes with periodic transcripts (~35%), and an even smaller fraction had transcripts with periodic translational efficiency (~6.5%) (Figure 4A). Overall, ~37% of the total periodic proteome displayed any type of periodicity at the level of gene expression (periodicity in either transcript level or translational efficiency). Interestingly, the periodic proteome for which we detected regulation at the level of gene expression was depleted for ribosome biogenesis proteins (false discovery rate [FDR]-adjusted p value: 2.77e−4). However, two recent studies that used methods enabling high intra-G1 resolution, reported that the abundance of transcripts encoding RPs increases and peaks during G1.[4,18] This finding is consistent with the overall trend that we observed in the concentration of RPs, with a prominent, coordinated increase during early to late G1 (Figures 3D and 3E).

For genes that were periodic in both transcript and protein concentration, we identified three general patterns of cell cycle-related transcript-protein dynamics. For most genes, we observed either a parallel change in transcript and protein levels (Figure 4B), or a change in transcript level followed shortly after by a change in the protein level (Figure 4C). However, a substantial number of genes had a large lag between changes in transcript and protein levels (Figure 4D). Genes with a large lag between transcript and protein dynamics showed no obvious bioprocess enrichment, whereas genes with a parallel change or short lag were enriched for glycosylation,

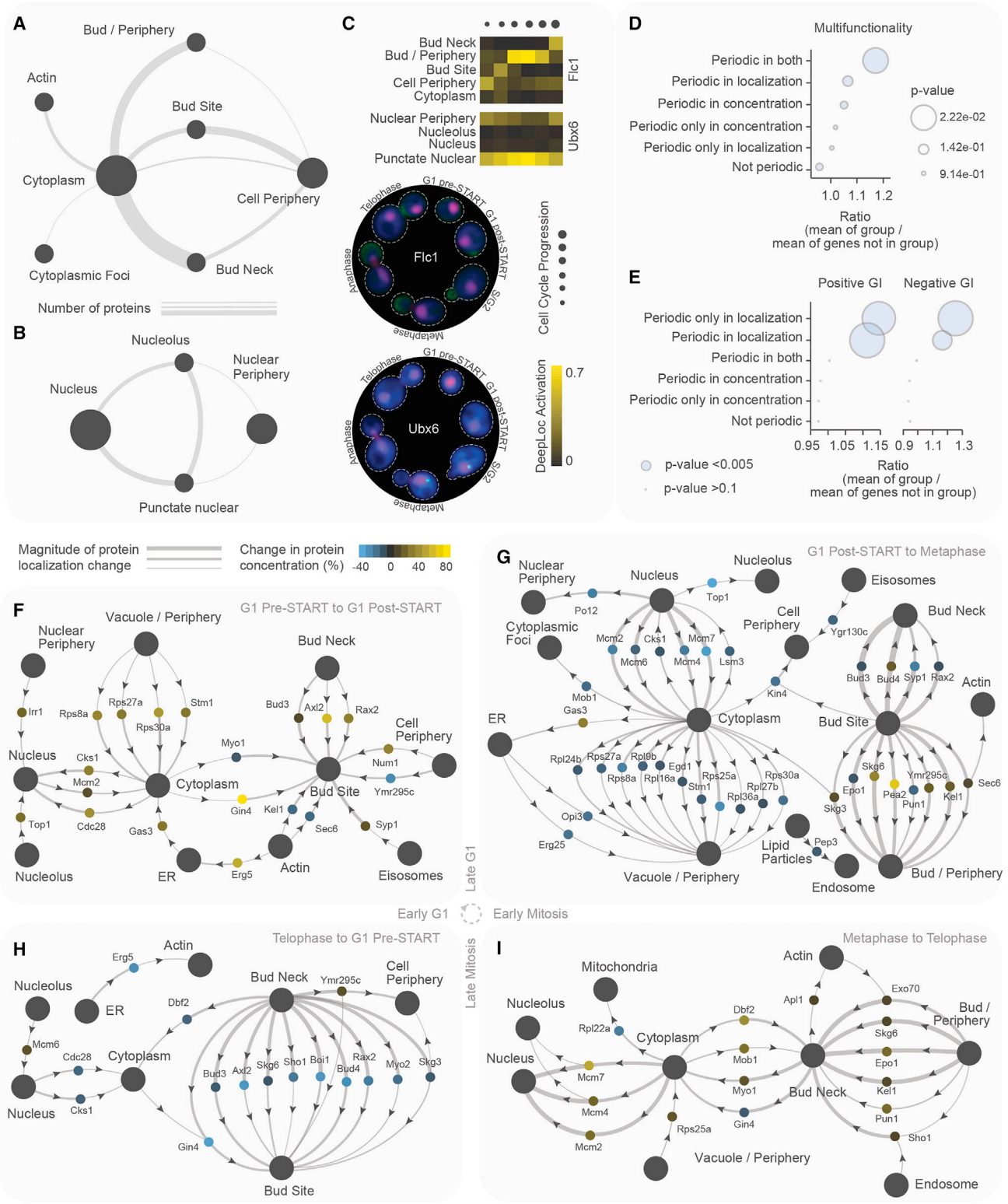

Figure 5. Spatiotemporal analysis of the cell cycle-periodic proteome

(A and B) Network diagram summarizing protein movements from larger toward more confined areas in the cytoplasm (A) or the nucleus (B) at any cell cycle stage. Edge thickness is proportional to the number of proteins moving between the indicated compartments. The large black nodes denote localization classes, and

(legend continued on next page)

protein folding/targeting, cell wall biosynthesis (fold-enrichment ~ 1.64, FDR-adjusted p value: 4.53e−2), and DNA replication and repair (fold-enrichment ~ 5.36, FDR-adjusted p value: 3.22e−4), respectively. Thus, in cases where the transcript of a protein with periodic concentration was also periodic, the concentration dynamics of the transcript were not always predictive of the protein dynamics.

As noted above, we were able to detect 213 transcripts that had periodic translational efficiency (Table S3), of which 101 were also periodic in their abundance (Table S3). We identified 32 genes with cell cycle-specific dynamics at all three levels (transcript concentration, translational efficiency, and protein concentration) (Table S3). These multi-level regulated genes were enriched specifically for annotations to the cell cycle process and its regulation (Table S3). Our list of translationally regulated transcripts included 33 cases of cell cycle genes for which periodicity in translational efficiency was not previously appreciated (Table S3; Figures 4E and S4E). Among those, 12 genes were regulated at all three levels, including *DBF2*, a positive regulator of mitotic exit,[82] and *ASE1*, which encodes a microtubule bundling protein required for spindle elongation and stability[83] (Figure 4E). Although the "tri-regulated" gene set is small, we saw various relationships between gene expression and protein dynamics, such as concurrent changes in transcript, translational efficiency, and protein levels (e.g., in the case of the subunit of the cohesin complex *MCD1*[84]), translational efficiency and protein levels increasing in parallel shortly after an increase in transcript levels (e.g., in the case of the cell polarity controller *GIC2*[85]), or protein levels following the changes in transcript and translational levels with a considerable lag (e.g., in the case of *ASE1*) (Figure 4E). Further analysis may reveal functional links between proteins that show these distinct patterns of regulation during the cell cycle.

Common features in proteome periodicity between the yeast and human cell division cycles

Our observation that most proteins whose concentration is cell cycle periodic are encoded by genes that are expressed continuously throughout the cell cycle has been seen consistently in yeast experiments,[4,18] and also in studies using human cells,[22] suggesting that multi-level regulation of protein concentrations is a common feature of the eukaryotic cell cycle. Furthermore, our dataset and others show that there is a substantial number of yeast transcripts with periodic abundance, for which no periodicity at the protein level is observed[4,18] (Figure 4A). In fact, in our dataset, we found that periodic transcripts for which no periodicity was observed at the protein level, changed in abundance during the cell cycle not negligibly, but significantly less in comparison to periodic transcripts for which there was detectable periodicity at the protein level (median change: ~1.77 and ~1.98, respectively; Mann-Whitney two-tailed p value = 0.0006).

We found further similarities between yeast and human cell cycle-resolved proteomes. Specifically, among the 539 proteins that were recently identified to have cell cycle-dependent profiles in human cells,[22] 166 have at least one yeast ortholog. In our study, we assessed at least one yeast ortholog for 133 out of this overlapping protein set and identified 45 that were periodic (Table S4). Thus, one-third of proteins that were identified as cell cycle-dependent in human cells and have yeast orthologs, are also cell cycle-dependent in yeast. Functional enrichment analysis indicated that both the yeast orthologs of the human cell cycle-dependent proteins (Figure S4F), and the fraction of them that is cell cycle-dependent also in yeast (Figure S4G), are involved in fundamental cell cycle-related bioprocesses. These findings suggest that the human and yeast cell division programs share similarities that extend beyond the stoichiometry of their regulatory networks,[86] to the dynamics of individual proteins.

Spatiotemporal analysis of the cell cycle-periodic proteome

As described earlier, we identified 405 proteins with periodic localization during the cell cycle, and 810 with periodic concentration, with only 133 of these proteins showing periodicity in both. This observation suggests that proteins are regulated most often either at the level of localization or concentration during the cell cycle, but not both, consistent with previous work.[25] Although only a small fraction of proteins changed both compartment localization and concentration during the cell cycle, we found sub-compartment localization changes may mediate local changes in protein concentration (Figures 5A–5C). Specifically, we identified 79 proteins that moved during the cell cycle toward more confined areas of the same compartment, such as from the whole cytosol to the bud site and the bud neck, or from the nuclear periphery to nuclear puncta (Figures 5A and 5B). Among these proteins, 50 were periodic only in localization. For example, the FAD transporter Flc1 did not display periodic concentration but moved from the cell periphery to the bud site, the bud and its periphery, and the bud neck, resulting in pronounced changes in its local concentration (Figure 5C). Similarly, the movement of the Cdc48-interacting protein Ubx6 from the nuclear periphery toward nuclear puncta caused periodic

their size reflects arbitrarily the physical size of the respective compartment. Specifically, large nodes depict the cytoplasm and the nucleus; smaller nodes their periphery; and the smallest nodes more physically confined areas within them, such as cytoplasmic or nuclear foci/puncta.

(C) Clustergram cross-sections and example micrographs (similar to Figure 1D) for two example proteins that show intra-compartmental movements (Flc1 and Ubx6).

(D and E) (D) Degree of multifunctionality and (E) involvement in genetic interactions of genes with the indicated periodicity patterns.

(F–I) Flux networks summarizing the cell cycle-periodic proteome. Localization classes are depicted as large gray nodes. Each protein is denoted by a small node, the color of which shows its concentration change at a particular cell cycle transition. Lines connect each protein node with the two localization classes for which change has been identified for this protein. Line thickness indicates the magnitude of the localization change, and the arrows indicate the directionality. For example, Gin4 increases in concentration from G1 Pre-START to G1 Post-START, and its localization decreases at the cytoplasm and increases at the bud site. Dynamics are depicted for G1 Pre-START to G1 Post-START (F), G1 Post-START to metaphase (G), metaphase to telophase (I), and telophase to G1 Pre-START (H).

See also Figure S5.

changes in its local concentration (Figure 5C) despite no significant periodicity in its overall concentration. Thus, intra-compartmental changes in protein localization can mediate local changes in protein concentration during the cell cycle, in the absence of significant changes in the total amount of the protein.

We assessed different groups of cell cycle-periodic proteins for functional enrichments or other features that may be more common among groups of proteins with a particular pattern of regulation. First, functional enrichment analysis of proteins that were periodic in concentration or localization, independently of the specific cell cycle phases where the changes were observed, revealed a preferential utilization of one specific mode of regulation over the other for different aspects of the cell cycle (Table S5). Specifically, proteins with periodic concentration were enriched almost exclusively for processes related to cell cycle control, whereas proteins with periodic localization for processes were mostly related to the biophysical implementation of the cell cycle program. In turn, proteins with periodicity in both concentration and localization were enriched for a more balanced mixture of these processes. Proteins with both periodic concentration and localization were also more likely to be multifunctional in comparison to non-periodic proteins or proteins that exhibited only one level of periodicity (Table S5; Figure 5D). Thus, multi-level regulation of protein abundance and localization may serve to target proteins to different cell cycle-specific functions.

By querying a database of over 46,000 phosphosites on budding yeast proteins,[87] we found that although a similar fraction of periodic and non-periodic proteins contained phosphosites (Figure S5A), proteins with periodicity in both localization and concentration contained significantly more phosphosites than non-periodic proteins or proteins that had only periodic concentration (Figure S5B). This observation suggests that cell cycle-specific phosphorylation may contribute to the observed periodicity and tendency for multifunctionality. Finally, despite multifunctionality being a feature of genes that are dense hubs in the genetic interaction network,[88] we found that only genes encoding proteins with periodic localization were involved in more genetic interactions than the average yeast gene (Table S5; Figure 5E), suggesting that the dynamic localization of proteins that are regulated at both the concentration and localization level is an important component of their multifunctionality.

Cell cycle-resolved phenomics for functional analysis and exploration of new biology

To better visualize the proteins that show both localization and concentration change with cell cycle position, we displayed them in flux networks that reflect proteome dynamics during major cell cycle transitions (Figures 5F–5I). In these maps, the movement of each protein (small nodes) from one localization class to another (large nodes), the magnitude of the respective localization change (arrow thickness), as well as the magnitude of the change in protein concentration (color-coding) are summarized in a cell cycle-resolved manner. For example, the flux network summarizing protein dynamics during G1 Pre-START to G1 PostSTART shows the protein kinase Gin4 moving from the cytoplasm to the bud site, with a parallel increase in concentration of ~80% (Figure 5F), whereas components of the Mcm2-7 complex move from the nucleus to the cytoplasm after cell cycle commitment, with a ~25% decrease in their concentration (Figure 5G).

Our flux network analysis revealed clear coordinated movement of proteins that was unanticipated. For example, proteins involved in cytoplasmic translation moved from the cytoplasm to the vacuole and/or its periphery after cell cycle commitment, and specifically, around metaphase, coincident with a decrease in their concentration (Figure 5G). This protein cluster included mostly RPs, as well the ribosome-associated protein Stm1.[89] We found that the degree of localization of a protein to the vacuole and/or its periphery at metaphase did not correlate with the fitness of the respective strain (Figures S5C and S5D), suggesting that this localization change is not related to interference of the GFP tag with protein function. This movement of proteins to the vacuole and/or its periphery was not always easily discernible via visual inspection (Figure S5E), potentially due to the high cytoplasmic abundance of RPs. However, among all highly abundant cytoplasmic proteins, DeepLoc predicted that it is specifically proteins involved in translation that move to the vacuole and/or its periphery at early mitosis (Figure S5F). The vacuolar periphery constitutes the primary residence of the central growth regulator TORC1, and the conditional residence of its effector Sch9, which is required for TORC1-mediated regulation of the translation machinery.[90,91] DeepLoc also predicted an increase in Sch9 localization to the vacuole and/or its periphery during metaphase (Figures S5G and S5H), suggesting that coordinated movement of translation-related proteins to the vacuole during the cell cycle may underlie physiologically relevant yet unexplored biology.

We were intrigued by the highly cell cycle-specific localization and concentration profile of a previously uncharacterized protein, Ymr295c (Figures 5F–5H). Previous studies demonstrated that Ymr295c localized to the polarized growth tip during budding and mating.[92] Our automated image analyses showed that Ymr295c localized at the cell periphery during early G1, to the bud tip in late G1, to the bud at S/G2, to the periphery of the bud at metaphase, and at the bud neck during telophase (Figure 6A), with concurrent changes in both its overall and local concentration (Table S1; Figure 6A). We found 40 proteins across our whole dataset with a localization profile similar to Ymr295c (Pearson's $r > 0.5$) (Figures 6B and S6B). These proteins were highly enriched for cell polarity and morphogenesis functions (Figure 6C; fold-enrichment: 9.755, FDR-adjusted p value: 6.1e−7), implicating Ymr295c in these bioprocesses. In particular, the flavin adenine dinucleotide transporter Flc1 showed the most similar localization profile to Ymr295c (Figure S6B), recapitulating all Ymr295c localization changes (Figures 5C and 6B), and it plays a key role in cell wall maintenance.[93]

Neither the deletion of *YMR295C*, nor the deletion of its uncharacterized paralog *YGR273C*, nor the deletion of both genes conferred any apparent fitness defect (Figure S6A). To test for phenotypes consistent with a role in cell wall regulation, we grew *ymr295cΔ* cells in conditions that cause cell wall stress, including heat shock, treatment with the N-glycosylation inhibitor tunicamycin (TN), and exposure to the antifungal drug caspofungin (CAS), which inhibits yeast 1,3-beta-glucan synthase.[96]

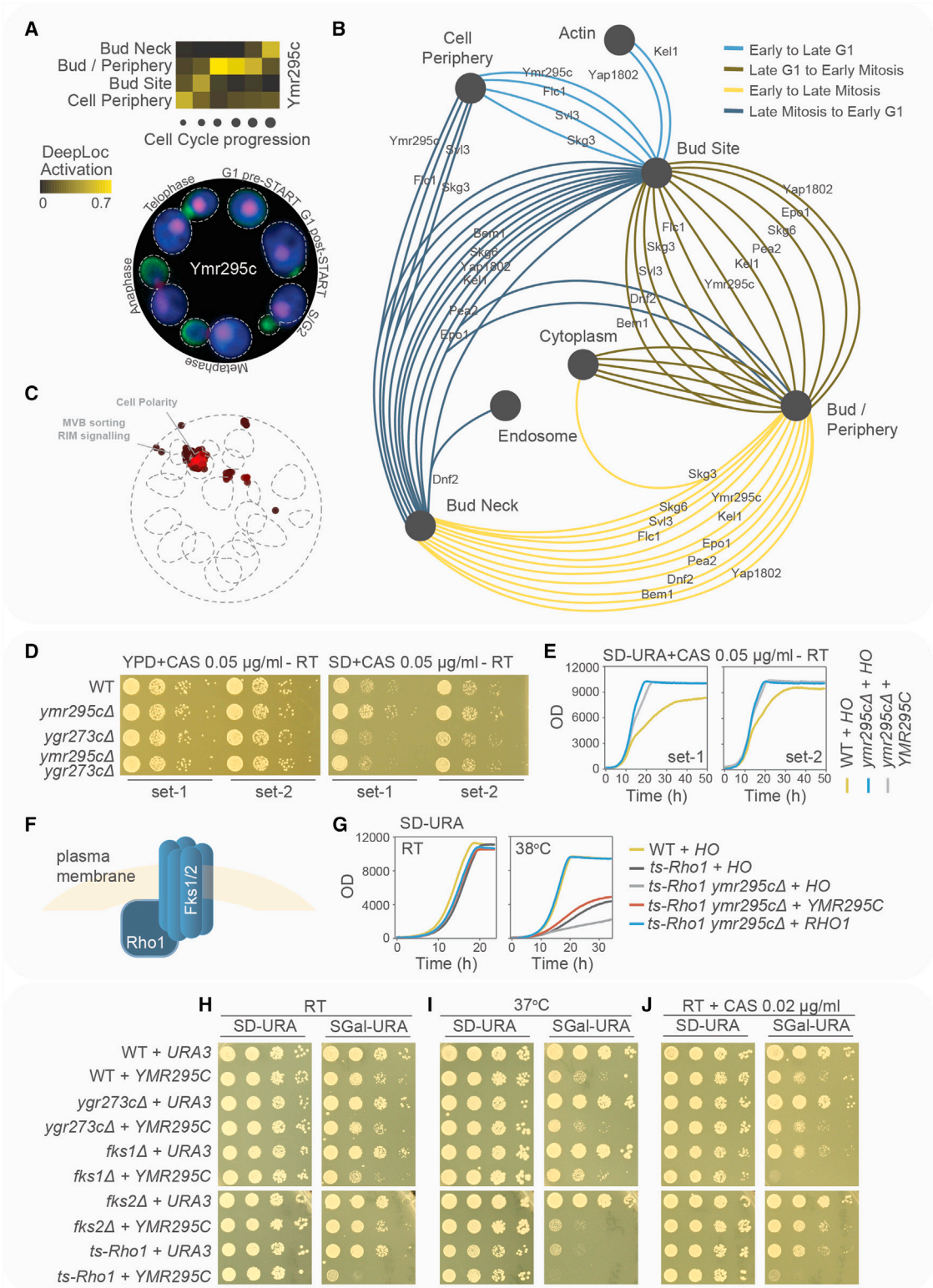

Figure 6. Cell cycle-resolved phenomics for functional analysis and exploration of new biology

(A) Clustergram cross-section and example micrographs (similar to Figure 1D) for Ymr295c.

(B) Map showing cell cycle-specific movements of the ten proteins with highest localization profile similarity to Ymr295c.

(legend continued on next page)

Although there was no effect of elevated temperature or TN treatment on the growth of *ymr295cΔ* cells (Figures S6C and S6D), *YMR295C* deletion partially rescued the CAS toxicity in synthetic medium (Figures 6D and 6E), supporting the hypothesis that Ymr295c is involved in cell morphogenesis, and specifically, cell wall formation.

To further explore the role of Ymr295c, we used the ubiquitin-based split-protein sensor assay[97] to screen for *in vivo* protein-protein interactions with Ymr295c, focusing on a matrix of 383 proteins known or suspected to be involved in different aspects of polarized growth in yeast (Table S6) (Figure S6E). The split-ubiquitin assay identified protein-protein interactions between Ymr295c and the 1,3-beta-glucan synthase proteins Fks1 and Fks2, as well as Rho1, which activates these synthases (Figures 6F and S6E). Finally, we tested for genetic interactions between *YMR295C* and these genes, and we identified a negative genetic interaction between *YMR295C* and *RHO1*, which was exacerbated in certain growth conditions (Figures 6G, S6F, and S6G).

Since Ymr295c was periodic both at the levels of localization and concentration, we asked whether constitutive overexpression of Ymr295c from the inducible galactose promoter might cause informative phenotypes. We found that *YMR295C* overexpression caused several phenotypes consistent with our previous observations: (1) a growth defect (Figure 6H), especially at high temperature (Figure 6I); (2) an exacerbation of the growth defect of a *rho1*ts strain (Figures 6H–6J); and (3) an additional negative genetic interaction between *YMR295C* and *FKS1* specific to the presence of CAS (Figure 6J). Moreover, *YMR295C* overexpression caused Ymr295c mis-localization (Figure S6H), and increased deposition of 1,3-beta-glucan at the sites where Ymr295c is normally localized (Figure S6I). Collectively, our phenomics-guided approach identifies Ymr295c as a previously unappreciated regulator of the biosynthesis of the main cell wall polysaccharide 1,3-beta-glucan, and we propose *GSR1* (glucan synthesis regulator) for its name.

Outlook

We generated a comprehensive map of molecular fluctuations occurring during the cell cycle of budding yeast. This map describes proteome-level dynamics in both concentration and localization during the cell cycle of live cells, with resolution of ~20 subcellular localization classes. Moreover, the spatiotemporal proteome data are supplemented by gene expression and translational efficiency data generated and scored under similar conditions. The comprehensive nature of this map offered by the high degree of spatial and temporal resolution and extensive proteome coverage, presents a resource that will facilitate the formulation and testing of cell cycle-related hypotheses at both the molecular and cellular levels. The experimental pipeline established here offers a paradigm of how systematic genetics, live cell microscopy, machine learning, and multi-omics integration can be utilized to dissect complex processes in eukaryotic systems. Moreover, the same pipeline can be directly applied to spatiotemporal analyses of the proteome under different genetic and environmental conditions, providing the opportunity to systematically survey factors that influence proteome dynamics in living cells.

Limitations of the study

Although our work provides cell cycle-resolved information about the dynamics of most of the yeast proteome, there is a fraction of mostly very low-abundance proteins that are challenging to detect by either GFP-based or label-free approaches. Methodological advancements permitting the systematic study of this set of proteins may provide useful new information about cell cycle regulation. Furthermore, although our proteome concentration and localization dynamics were measured on the same cells, we relied on combining data from synchronized cell populations to measure transcript and translation levels. Ideally, multi-omics cell cycle-resolved data would be assessed on the same single cells, which although challenging to implement on a genome scale, may be possible with advances in single-cell assays for translation,[98] transcriptomes,[99] and metabolomes.[100]

STAR★METHODS

Detailed methods are provided in the online version of this paper and include the following:

- KEY RESOURCES TABLE
- RESOURCE AVAILABILITY
  - Lead contact
  - Materials availability
  - Data and code availability
- EXPERIMENTAL MODEL AND STUDY PARTICIPANT DETAILS
  - Yeast Strains for Microscopy Experiments
  - Yeast Strains for Sequencing Experiments
  - Yeast Strains for *YMR295C* characterization
- METHOD DETAILS
  - Cell cycle proteomics
  - Cell cycle gene expression & translational efficiency
  - YMR295C CHARACTERIZATION

(C) Spatial analysis of functional enrichment (SAFE) analysis for proteins (n = 40) with similar (Pearson's r ≥ 0.5) cell cycle-specific localization profile to Ymr295c. The dotted shapes on the map indicate the bioprocesses enriched on the global similarity network of yeast genetic interactions (GIs)[88] (thecellmap.com).
(D) Spot dilution assays on YPD and SD media for the indicated strains in the presence of caspofungin (CAS). Set-1 and Set-2 denote spots initiated from different precultures (RT, room temperature).
(E) Growth assays of wild-type (WT) and *ymr295cΔ* liquid cultures in the presence of CAS, with cells expressing either *HO* or *YMR295C* via a MoBY plasmid.[94]
(F) Schematic representation of the 1,3-beta-glucan synthase complex.
(G) Complementation assays from liquid cultures of the indicated strains expressing *HO*, *YMR295C*, or *RHO1*, via a MoBY plasmid[94] at RT or 38°C.
(H–J) Spot dilution assays of WT and the indicated deletion strains carrying either a Gal-induced *URA3* or *YMR295C* plasmid[95] at (H) RT, (I) 37°C, and (J) RT with CAS.
See also Figure S6.

- Non-dataset-specific information
- QUANTIFICATION AND STATISTICAL ANALYSIS

SUPPLEMENTAL INFORMATION

Supplemental information can be found online at https://doi.org/10.1016/j.cell.2024.02.014.

ACKNOWLEDGMENTS

We thank M. Costanzo, C. Yeung, and members of the Andrews and Boone labs for helpful discussions and M. Usaj for preliminary work on the cell cycle viewer. This work was supported by grants from the National Institutes of Health (R01HG005853 to B.J.A. and C.B.), and the Canadian Institutes of Health Research (PJT-180259 to B.J.A.). We gratefully acknowledge the support of NVIDIA Corporation with the donation of the Titan Xp GPU used for this research. Equipment for automated image acquisition and analysis was purchased using funds from the Canadian Foundation for Innovation and the Ontario Research Fund. A.L. holds a CIHR Fellowship (MFE - 187913). Work in the Johnsson lab was supported by a grant from the DFG Jo 187/9-1. C.B. is a CIFAR Fellow, and B.J.A. holds a Tier 1 Canada Research Chair in Systems Genetics and Cell Biology.

AUTHOR CONTRIBUTIONS

A.L. and B.T.G. designed and performed experiments, analyzed data, and wrote the paper. O.Z.K. developed CycleNet and DeepLoc and performed computational analyses. H.F. designed and performed experiments. C.R., D.T.F., M.B., and C.M. performed additional data analysis. M.P.D.M. developed the database, image viewer, and cell cycle viewer for TheCellVision.org website. S.T. and M.T.C. performed additional experiments, while N.J. and L.S.C. supervised them. B.J.A. and C.B. supervised the project and wrote the paper.

DECLARATION OF INTERESTS

The authors declare no competing interests.

Received: September 12, 2023
Revised: December 1, 2023
Accepted: February 12, 2024
Published: March 6, 2024

REFERENCES

1. Williams, G.H., and Stoeber, K. (2012). The cell cycle and cancer. J. Pathol. *226*, 352–364.
2. Joseph, C., Mangani, A.S., Gupta, V., Chitranshi, N., Shen, T., Dheer, Y., Kb, D., Mirzaei, M., You, Y., Graham, S.L., et al. (2020). Cell Cycle Deficits in Neurodegenerative Disorders: Uncovering Molecular Mechanisms to Drive Innovative Therapeutic Development. Aging Dis. *11*, 946–966.
3. Crosby, M.E. (2007). Cell Cycle: Principles of Control. Yale J. Biol. Med. *80*, 141.
4. Blank, H.M., Papoulas, O., Maitra, N., Garge, R., Kennedy, B.K., Schilling, B., Marcotte, E.M., and Polymenis, M. (2020). Abundances of transcripts, proteins, and metabolites in the cell cycle of budding yeast reveal coordinate control of lipid metabolism. Mol. Biol. Cell *31*, 1069–1084.
5. Whitfield, M.L., Sherlock, G., Saldanha, A.J., Murray, J.I., Ball, C.A., Alexander, K.E., Matese, J.C., Perou, C.M., Hurt, M.M., Brown, P.O., et al. (2002). Identification of genes periodically expressed in the human cell cycle and their expression in tumors. Mol. Biol. Cell *13*, 1977–2000.
6. Bar-Joseph, Z., Siegfried, Z., Brandeis, M., Brors, B., Lu, Y., Eils, R., Dynlacht, B.D., and Simon, I. (2008). Genome-wide transcriptional analysis of the human cell cycle identifies genes differentially regulated in normal and cancer cells. Proc. Natl. Acad. Sci. USA *105*, 955–960.
7. Orlando, D.A., Lin, C.Y., Bernard, A., Wang, J.Y., Socolar, J.E., Iversen, E.S., Hartemink, A.J., and Haase, S.B. (2008). Global control of cell-cycle transcription by coupled CDK and network oscillators. Nature *453*, 944–947.
8. Grant, G.D., Brooks, L., Zhang, X., Mahoney, J.M., Martyanov, V., Wood, T.A., Sherlock, G., Cheng, C., and Whitfield, M.L. (2013). Identification of cell cycle-regulated genes periodically expressed in U2OS cells and their regulation by FOXM1 and E2F transcription factors. Mol. Biol. Cell *24*, 3634–3650.
9. Ly, T., Ahmad, Y., Shlien, A., Soroka, D., Mills, A., Emanuele, M.J., Stratton, M.R., and Lamond, A.I. (2014). A proteomic chronology of gene expression through the cell cycle in human myeloid leukemia cells. eLife *3*, e01630.
10. Ly, T., Whigham, A., Clarke, R., Brenes-Murillo, A.J., Estes, B., Madhessian, D., Lundberg, E., Wadsworth, P., and Lamond, A.I. (2017). Proteomic analysis of cell cycle progression in asynchronous cultures, including mitotic subphases, using PRIMMUS. eLife *6*, e27574.
11. Dominguez, D., Tsai, Y.H., Gomez, N., Jha, D.K., Davis, I., and Wang, Z. (2016). A high-resolution transcriptome map of cell cycle reveals novel connections between periodic genes and cancer. Cell Res. *26*, 946–962.
12. Kelliher, C.M., Leman, A.R., Sierra, C.S., and Haase, S.B. (2016). Investigating Conservation of the Cell-Cycle-Regulated Transcriptional Program in the Fungal Pathogen, Cryptococcus neoformans. PLoS Genet. *12*, e1006453.
13. Boström, J., Sramkova, Z., Salašová, A., Johard, H., Mahdessian, D., Fedr, R., Marks, C., Medalová, J., Souček, K., Lundberg, E., et al. (2017). Comparative cell cycle transcriptomics reveals synchronization of developmental transcription factor networks in cancer cells. PLoS One *12*, e0188772.
14. Herr, P., Boström, J., Rullman, E., Rudd, S.G., Vesterlund, M., Lehtiö, J., Helleday, T., Maddalo, G., and Altun, M. (2020). Cell Cycle Profiling Reveals Protein Oscillation, Phosphorylation, and Localization Dynamics. Mol. Cell. Proteomics *19*, 608–623.
15. Lee, H.J., Jedrychowski, M.P., Vinayagam, A., Wu, N., Shyh-Chang, N., Hu, Y., Min-Wen, C., Moore, J.K., Asara, J.M., Lyssiotis, C.A., et al. (2017). Proteomic and Metabolomic Characterization of a Mammalian Cellular Transition from Quiescence to Proliferation. Cell Rep. *20*, 721–736.
16. Teufel, L., Tummler, K., Flöttmann, M., Herrmann, A., Barkai, N., and Klipp, E. (2019). A transcriptome-wide analysis deciphers distinct roles of G1 cyclins in temporal organization of the yeast cell cycle. Sci. Rep. *9*, 3343.
17. Roci, I., Watrous, J.D., Lagerborg, K.A., Jain, M., and Nilsson, R. (2020). Mapping metabolic oscillations during cell cycle progression. Cell Cycle *19*, 2676–2684.
18. Campbell, K., Westholm, J., Kasvandik, S., Di Bartolomeo, F., Mormino, M., and Nielsen, J. (2020). Building blocks are synthesized on demand during the yeast cell cycle. Proc. Natl. Acad. Sci. USA *117*, 7575–7583.
19. Rossio, V., and Paulo, J.A. (2022). Quantitative proteome and phosphoproteome datasets of DNA replication and mitosis in Saccharomyces cerevisiae. Data Brief *45*, 108741.
20. Kelliher, C.M., Foster, M.W., Motta, F.C., Deckard, A., Soderblom, E.J., Moseley, M.A., and Haase, S.B. (2018). Layers of regulation of cell-cycle gene expression in the budding yeast Saccharomyces cerevisiae. Mol. Biol. Cell *29*, 2644–2655.
21. Farkash-Amar, S., Eden, E., Cohen, A., Geva-Zatorsky, N., Cohen, L., Milo, R., Sigal, A., Danon, T., and Alon, U. (2012). Dynamic Proteomics of Human Protein Level and Localization across the Cell Cycle. PLoS One *7*, e48722.
22. Mahdessian, D., Cesnik, A.J., Gnann, C., Danielsson, F., Stenström, L., Arif, M., Zhang, C., Le, T., Johansson, F., Schutten, R., et al. (2021). Spatiotemporal dissection of the cell cycle with single-cell proteogenomics. Nature *590*, 649–654.

23. Huh, W.K., Falvo, J.V., Gerke, L.C., Carroll, A.S., Howson, R.W., Weissman, J.S., and O'Shea, E.K. (2003). Global analysis of protein localization in budding yeast. Nature *425*, 686–691.

24. Kraus, O.Z., Grys, B.T., Ba, J., Chong, Y., Frey, B.J., Boone, C., and Andrews, B.J. (2017). Automated analysis of high-content microscopy data with deep learning. Mol. Syst. Biol. *13*, 924.

25. Chong, Y.T., Koh, J.L., Friesen, H., Duffy, S.K., Cox, M.J., Moses, A., Moffat, J., Boone, C., and Andrews, B.J. (2015). Yeast Proteome Dynamics from Single Cell Imaging and Automated Analysis. Cell *161*, 1413–1424.

26. Tkach, J.M., Yimit, A., Lee, A.Y., Riffle, M., Costanzo, M., Jaschob, D., Hendry, J.A., Ou, J., Moffat, J., Boone, C., et al. (2012). Dissecting DNA damage response pathways by analysing protein localization and abundance changes during DNA replication stress. Nat. Cell Biol. *14*, 966–976.

27. Ho, B., Baryshnikova, A., and Brown, G.W. (2018). Unification of Protein Abundance Datasets Yields a Quantitative Saccharomyces cerevisiae Proteome. Cell Syst. *6*, 192–205.e3.

28. Tong, A.H.Y., Evangelista, M., Parsons, A.B., Xu, H., Bader, G.D., Pagé, N., Robinson, M., Raghibizadeh, S., Hogue, C.W., Bussey, H., et al. (2001). Systematic genetic analysis with ordered arrays of yeast deletion mutants. Science *294*, 2364–2368.

29. Deckard, A., Anafi, R.C., Hogenesch, J.B., Haase, S.B., and Harer, J. (2013). Design and analysis of large-scale biological rhythm studies: a comparison of algorithms for detecting periodic signals in biological data. Bioinformatics *29*, 3174–3180.

30. Lomb, N.R. (1976). Least-squares frequency analysis of unequally spaced data. Astrophys. Space Sci. *39*, 447–462.

31. Scargle, J.D. (1982). Studies in astronomical time series analysis. II - Statistical aspects of spectral analysis of unevenly spaced data. Astrophys. J. *263*, 835.

32. de Lichtenberg, U., Jensen, L.J., Fausbøll, A., Jensen, T.S., Bork, P., and Brunak, S. (2005). Comparison of computational methods for the identification of cell cycle-regulated genes. Bioinformatics *21*, 1164–1171.

33. Cohen-Steiner, D., Edelsbrunner, H., Harer, J., and Mileyko, Y. (2010). Lipschitz Functions Have L p -Stable Persistence. Found. Comput. Math. *10*, 127–139.

34. Hughes, M.E., Hogenesch, J.B., and Kornacker, K. (2010). JTK_CYCLE: an efficient nonparametric algorithm for detecting rhythmic components in genome-scale data sets. J. Biol. Rhythms *25*, 372–380.

35. Costanzo, M., Nishikawa, J.L., Tang, X., Millman, J.S., Schub, O., Breitkreuz, K., Dewar, D., Rupes, I., Andrews, B., and Tyers, M. (2004). CDK activity antagonizes Whi5, an inhibitor of G1/S transcription in yeast. Cell *117*, 899–913.

36. Cvrcková, F., De Virgilio, C., Manser, E., Pringle, J.R., and Nasmyth, K. (1995). Ste20-like protein kinases are required for normal localization of cell growth and for cytokinesis in budding yeast. Genes Dev. *9*, 1817–1830.

37. Zanelli, C.F., and Valentini, S.R. (2005). Pkc1 Acts Through Zds1 and Gic1 to Suppress Growth and Cell Polarity Defects of a Yeast eIF5A Mutant. Genetics *171*, 1571–1581.

38. Hennessy, K.M., Clark, C.D., and Botstein, D. (1990). Subcellular localization of yeast CDC46 varies with the cell cycle. Genes Dev. *4*, 2252–2263.

39. Chen, Y., Hennessy, K.M., Botstein, D., and Tye, B.K. (1992). CDC46/MCM5, a yeast protein whose subcellular localization is cell cycle-regulated, is involved in DNA replication at autonomously replicating sequences. Proc. Natl. Acad. Sci. USA *89*, 10459–10463.

40. Dalton, S., and Whitbread, L. (1995). Cell cycle-regulated nuclear import and export of Cdc47, a protein essential for initiation of DNA replication in budding yeast. Proc. Natl. Acad. Sci. USA *92*, 2514–2518.

41. Holly, S.P., and Blumer, K.J. (1999). PAK-Family Kinases Regulate Cell and Actin Polarization throughout the Cell Cycle of Saccharomyces cerevisiae. J. Cell Biol. *147*, 845–856.

42. Songer, J.A., and Munson, M. (2009). Sec6p Anchors the Assembled Exocyst Complex at Sites of Secretion. Mol. Biol. Cell *20*, 973–982.

43. Meitinger, F., Richter, H., Heisel, S., Hub, B., Seufert, W., and Pereira, G. (2013). A Safeguard Mechanism Regulates Rho GTPases to Coordinate Cytokinesis with the Establishment of Cell Polarity. PLoS Biol. *11*, e1001495.

44. Chapa-y-Lazo, B., Allwood, E.G., Smaczynska-de Rooij, I.I., Snape, M.L., and Ayscough, K.R. (2014). Yeast Endocytic Adaptor AP-2 Binds the Stress Sensor Mid2 and Functions in Polarized Cell Responses. Traffic *15*, 546–557.

45. Freeman, L., Aragon-Alcaide, L., and Strunnikov, A. (2000). The Condensin Complex Governs Chromosome Condensation and Mitotic Transmission of rDNA. J. Cell Biol. *149*, 811–824.

46. Reynard, G.J., Reynolds, W., Verma, R., and Deshaies, R.J. (2000). Cks1 Is Required for G1 Cyclin–Cyclin-Dependent Kinase Activity in Budding Yeast. Mol. Cell. Biol. *20*, 5858–5864.

47. Wang, H., Garí, E., Vergés, E., Gallego, C., and Aldea, M. (2004). Recruitment of Cdc28 by Whi3 restricts nuclear accumulation of the G1 cyclin-Cdk complex to late G1. EMBO J. *23*, 180–190.

48. Drees, B.L., Sundin, B., Brazeau, E., Caviston, J.P., Chen, G.C., Guo, W., Kozminski, K.G., Lau, M.W., Moskow, J.J., Tong, A., et al. (2001). A protein interaction map for cell polarity development. J. Cell Biol. *154*, 549–571.

49. Ho, Y., Gruhler, A., Heilbut, A., Bader, G.D., Moore, L., Adams, S.L., Millar, A., Taylor, P., Bennett, K., Boutilier, K., et al. (2002). Systematic identification of protein complexes in Saccharomyces cerevisiae by mass spectrometry. Nature *415*, 180–183.

50. Kazuko, I., Moriyama, K., Matsumoto, S., Kawasaki, H., Nishida, E., and Yahara, I. (1993). Isolation of a yeast essential gene, COF1, that encodes a homologue of mammalian cofilin, a low-Mr actin-binding and depolymerizing protein. Gene *124*, 115–120.

51. Curwin, A.J., von Blume, J., and Malhotra, V. (2012). Cofilin-mediated sorting and export of specific cargo from the Golgi apparatus in yeast. Mol. Biol. Cell *23*, 2327–2338.

52. Shaw, J.A., Mol, P.C., Bowers, B., Silverman, S.J., Valdivieso, M.H., Durán, A., and Cabib, E. (1991). The function of chitin synthases 2 and 3 in the Saccharomyces cerevisiae cell cycle. J. Cell Biol. *114*, 111–123.

53. Trilla, J.A., Durán, A., and Roncero, C. (1999). Chs7p, a new protein involved in the control of protein export from the endoplasmic reticulum that is specifically engaged in the regulation of chitin synthesis in Saccharomyces cerevisiae. J. Cell Biol. *145*, 1153–1163.

54. Masinas, M.P.D., Usaj, M.M., Usaj, M., Boone, C., and Andrews, B.J. (2020). TheCellVision.org: A Database for Visualizing and Mining High-Content Cell Imaging Projects. G3 (Bethesda) *10*, 3969–3976.

55. Newman, J.R.S., Ghaemmaghami, S., Ihmels, J., Breslow, D.K., Noble, M., DeRisi, J.L., and Weissman, J.S. (2006). Single-cell proteomic analysis of S. cerevisiae reveals the architecture of biological noise. Nature *441*, 840–846.

56. Heim, R., Cubitt, A.B., and Tsien, R.Y. (1995). Improved green fluorescence. Nature *373*, 663–664.

57. Iizuka, R., Yamagishi-Shirasaki, M., and Funatsu, T. (2011). Kinetic study of de novo chromophore maturation of fluorescent proteins. Anal. Biochem. *414*, 173–178.

58. Marguerat, S., and Bähler, J. (2012). Coordinating genome expression with cell size. Trends Genet. *28*, 560–565.

59. Schmoller, K.M., Turner, J.J., Kõivomägi, M., and Skotheim, J.M. (2015). Dilution of the cell cycle inhibitor Whi5 controls budding-yeast cell size. Nature *526*, 268–272.

60. Litsios, A., Huberts, D.H.E.W., Terpstra, H.M., Guerra, P., Schmidt, A., Buczak, K., Papagiannakis, A., Rovetta, M., Hekelaar, J., Hubmann,

G., et al. (2019). Differential scaling between G1 protein production and cell size dynamics promotes commitment to the cell division cycle in budding yeast. Nat. Cell Biol. *21*, 1382–1392.

61. Sommer, R.A., DeWitt, J.T., Tan, R., and Kellogg, D.R. (2021). Growth-dependent signals drive an increase in early g1 cyclin concentration to link cell cycle entry with cell growth. eLife *10*, e64364.
62. Dorsey, S., Tollis, S., Cheng, J., Black, L., Notley, S., Tyers, M., and Royer, C.A. (2018). G1/S Transcription Factor Copy Number Is a Growth-Dependent Determinant of Cell Cycle Commitment in Yeast. Cell Syst. *6*, 539–554.e11.
63. Black, L., Tollis, S., Fu, G., Fiche, J.B., Dorsey, S., Cheng, J., Ghazal, G., Notley, S., Crevier, B., Bigness, J., et al. (2020). G1/S transcription factors assemble in increasing numbers of discrete clusters through G1 phase. J. Cell Biol. *219*, e202003041.
64. Litsios, A., Goswami, P., Terpstra, H.M., Coffin, C., Vuillemenot, L.A., Rovetta, M., Ghazal, G., Guerra, P., Buczak, K., Schmidt, A., et al. (2022). The timing of Start is determined primarily by increased synthesis of the Cln3 activator rather than dilution of the Whi5 inhibitor. Mol. Biol. Cell *33*, rp2.
65. Tollis, S. (2022). The G1/S repressor WHI5 is expressed at similar levels throughout the cell cycle. BMC Res. Notes *15*, 248.
66. Guerra, P., Vuillemenot, L.P.E., van Oppen, Y.B., Been, M., and Milias-Argeitis, A. (2022). TORC1 and PKA activity towards ribosome biogenesis oscillates in synchrony with the budding yeast cell cycle. J. Cell Sci. *135*, jcs260378.
67. Monteiro, F., Hubmann, G., Takhaveev, V., Vedelaar, S.R., Norder, J., Hekelaar, J., Saldida, J., Litsios, A., Wijma, H.J., Schmidt, A., et al. (2019). Measuring glycolytic flux in single yeast cells with an orthogonal synthetic biosensor. Mol. Syst. Biol. *15*, e9071.
68. Faergeman, N.J., DiRusso, C.C., Elberger, A., Knudsen, J., and Black, P.N. (1997). Disruption of the Saccharomyces cerevisiae homologue to the murine fatty acid transport protein impairs uptake and growth on long-chain fatty acids. J. Biol. Chem. *272*, 8531–8538.
69. Watkins, P.A., Lu, J.F., Steinberg, S.J., Gould, S.J., Smith, K.D., and Braiterman, L.T. (1998). Disruption of the Saccharomyces cerevisiae FAT1 gene decreases very long-chain fatty acyl-CoA synthetase activity and elevates intracellular very long-chain fatty acid concentrations. J. Biol. Chem. *273*, 18210–18219.
70. Choi, J.Y., and Martin, C.E. (1999). The Saccharomyces cerevisiae FAT1 Gene Encodes an Acyl-CoA Synthetase That Is Required for Maintenance of Very Long Chain Fatty Acid Levels. J. Biol. Chem. *274*, 4671–4683.
71. Zou, Z., DiRusso, C.C., Ctrnacta, V., and Black, P.N. (2002). Fatty acid transport in Saccharomyces cerevisiae. Directed mutagenesis of FAT1 distinguishes the biochemical activities associated with Fat1p. J. Biol. Chem. *277*, 31062–31071.
72. Claus, S., Jezierska, S., and Van Bogaert, I.N.A. (2019). Protein-facilitated transport of hydrophobic molecules across the yeast plasma membrane. FEBS Lett. *593*, 1508–1527.
73. Schwob, E., Böhm, T., Mendenhall, M.D., and Nasmyth, K. (1994). The B-type cyclin kinase inhibitor p40SIC1 controls the G1 to S transition in S. cerevisiae. Cell *79*, 233–244.
74. Pramila, T., Wu, W., Miles, S., Noble, W.S., and Breeden, L.L. (2006). The Forkhead transcription factor Hcm1 regulates chromosome segregation genes and fills the S-phase gap in the transcriptional circuitry of the cell cycle. Genes Dev. *20*, 2266–2278.
75. Lu, Y., and Cross, F.R. (2010). Periodic cyclin-cdk activity entrains an autonomous cdc14 release oscillator. Cell *141*, 268–279.
76. Ghiara, J.B., Richardson, H.E., Sugimoto, K., Henze, M., Lew, D.J., Wittenberg, C., and Reed, S.I. (1991). A Cyclin B Homolog in S. cerevisiae: Chronic Activation of the Cdc28 Protein Kinase by Cyclin Prevents Exit from Mitosis. Cell *65*, 163–174.
77. Bobola, N., Jansen, R.P., Shin, T.H., and Nasmyth, K. (1996). Asymmetric Accumulation of Ash1p in Postanaphase Nuclei Depends on a Myosin and Restricts Yeast Mating-Type Switching to Mother Cells. Cell *84*, 699–709.
78. Ingolia, N.T., Ghaemmaghami, S., Newman, J.R., and Weissman, J.S. (2009). Genome-wide analysis in vivo of translation with nucleotide resolution using ribosome profiling. Science *324*, 218–223.
79. Spellman, P.T., Sherlock, G., Zhang, M.Q., Iyer, V.R., Anders, K., Eisen, M.B., Brown, P.O., Botstein, D., and Futcher, B. (1998). Comprehensive identification of cell cycle-regulated genes of the yeast Saccharomyces cerevisiae by microarray hybridization. Mol. Biol. Cell *9*, 3273–3297.
80. Granovskaia, M.V., Jensen, L.J., Ritchie, M.E., Toedling, J., Ning, Y., Bork, P., Huber, W., and Steinmetz, L.M. (2010). High-resolution transcription atlas of the mitotic cell cycle in budding yeast. Genome Biol. *11*, R24.
81. Krzywinski, M., Schein, J., Birol, I., Connors, J., Gascoyne, R., Horsman, D., Jones, S.J., and Marra, M.A. (2009). Circos: An information aesthetic for comparative genomics. Genome Res. *19*, 1639–1645.
82. Oh, Y., Chang, K.J., Orlean, P., Wloka, C., Deshaies, R., and Bi, E. (2012). Mitotic exit kinase Dbf2 directly phosphorylates chitin synthase Chs2 to regulate cytokinesis in budding yeast. Mol. Biol. Cell *23*, 2445–2456.
83. Pellman, D., Bagget, M., Tu, Y.H., Fink, G.R., and Tu, H. (1995). Two microtubule-associated proteins required for anaphase spindle movement in Saccharomyces cerevisiae. J. Cell Biol. *130*, 1373–1385.
84. Guacci, V., Koshland, D., and Strunnikov, A. (1997). A direct link between sister chromatid cohesion and chromosome condensation revealed through the analysis of MCD1 in S. cerevisiae. Cell *91*, 47–57.
85. Brown, J.L., Jaquenoud, M., Gulli, M.P., Chant, J., and Peter, M. (1997). Novel Cdc42-binding proteins Gic1 and Gic2 control cell polarity in yeast. Genes Dev. *11*, 2972–2982.
86. Harashima, H., Dissmeyer, N., and Schnittger, A. (2013). Cell cycle control across the eukaryotic kingdom. Trends Cell Biol. *23*, 345–356.
87. Lanz, M.C., Yugandhar, K., Gupta, S., Sanford, E.J., Faça, V.M., Vega, S., Joiner, A.M.N., Fromme, J.C., Yu, H., and Smolka, M.B. (2021). In-depth and 3-dimensional exploration of the budding yeast phosphoproteome. EMBO Rep. *22*, e51121.
88. Costanzo, M., VanderSluis, B., Koch, E.N., Baryshnikova, A., Pons, C., Tan, G., Wang, W., Usaj, M., Hanchard, J., Lee, S.D., et al. (2016). A global genetic interaction network maps a wiring diagram of cellular function. Science *353*, aaf1420.
89. Van Dyke, N., Baby, J., and Van Dyke, M.W. (2006). Stm1p, a Ribosome-associated Protein, is Important for Protein Synthesis in Saccharomyces cerevisiae under Nutritional Stress Conditions. J. Mol. Biol. *358*, 1023–1031.
90. Loewith, R. (2010). TORC1 Signaling in Budding Yeast. Enzymes (Essen) *27*, 147–175.
91. Novarina, D., Guerra, P., and Milias-Argeitis, A. (2021). Vacuolar Localization via the N-terminal Domain of Sch9 is Required for TORC1-dependent Phosphorylation and Downstream Signal Transduction. J. Mol. Biol. *433*, 167326.
92. Narayanaswamy, R., Moradi, E.K., Niu, W., Hart, G.T., Davis, M., McGary, K.L., Ellington, A.D., and Marcotte, E.M. (2009). Systematic Definition of Protein Constituents along the Major Polarization Axis Reveals an Adaptive Reuse of the Polarization Machinery in Pheromone-Treated Budding Yeast. J. Proteome Res. *8*, 6–19.
93. Protchenko, O., Rodriguez-Suarez, R., Androphy, R., Bussey, H., and Philpott, C.C. (2006). A Screen for Genes of Heme Uptake Identifies the FLC Family Required for Import of FAD into the Endoplasmic Reticulum. J. Biol. Chem. *281*, 21445–21457.
94. Ho, C.H., Magtanong, L., Barker, S.L., Gresham, D., Nishimura, S., Natarajan, P., Koh, J.L.Y., Porter, J., Gray, C.A., Andersen, R.J., et al. (2009). A molecular barcoded yeast ORF library enables mode-of-action analysis of bioactive compounds. Nat. Biotechnol. *27*, 369–377.

95. Sopko, R., Huang, D., Preston, N., Chua, G., Papp, B., Kafadar, K., Snyder, M., Oliver, S.G., Cyert, M., Hughes, T.R., et al. (2006). Mapping pathways and phenotypes by systematic gene overexpression. Mol. Cell *21*, 319–330.

96. Denning, D.W. (2003). Echinocandin antifungal drugs. Lancet *362*, 1142–1151.

97. Johnsson, N., and Varshavsky, A. (1994). Split ubiquitin as a sensor of protein interactions in vivo. Proc. Natl. Acad. Sci. USA *91*, 10340–10344.

98. Zeng, H., Huang, J., Ren, J., Wang, C.K., Tang, Z., Zhou, H., Zhou, Y., Shi, H., Aditham, A., Sui, X., et al. (2023). Spatially resolved single-cell translatomics at molecular resolution. Science *380*, eadd3067.

99. Kanter, I., and Kalisky, T. (2015). Single cell transcriptomics: methods and applications. Front. Oncol. *5*, 53.

100. Seydel, C. (2021). Single-cell metabolomics hits its stride. Nat. Methods *18*, 1452–1456.

101. Brachmann, C.B., Davies, A., Cost, G.J., Caputo, E., Li, J., Hieter, P., and Boeke, J.D. (1998). Designer deletion strains derived from Saccharomyces cerevisiae S288C: a useful set of strains and plasmids for PCR-mediated gene disruption and other applications. Yeast *14*, 115–132.

102. Giaever, G., Chu, A.M., Ni, L., Connelly, C., Riles, L., Véronneau, S., Dow, S., Lucau-Danila, A., Anderson, K., André, B., et al. (2002). Functional profiling of the Saccharomyces cerevisiae genome. Nature *418*, 387–391.

103. Dünkler, A., Müller, J., and Johnsson, N. (2012). Detecting protein-protein interactions with the Split-ubiquitin sensor. Methods Mol. Biol. *786*, 115–130.

104. Schneider, C.A., Rasband, W.S., and Eliceiri, K.W. (2012). NIH Image to ImageJ: 25 years of image analysis. Nat. Methods *9*, 671–675.

105. Sheff, M.A., and Thorn, K.S. (2004). Optimized cassettes for fluorescent protein tagging in Saccharomyces cerevisiae. Yeast *21*, 661–670.

106. Beucher, S. (1992). The Watershed Transformation Applied to Image Segmentation. Scan. Microsc. *6*, 28.

107. Adams, R., and Bischof, L. (1994). Seeded Region Growing. IEEE Trans. Pattern Anal. Mach. Intell. *16*, 641–647.

108. Bengtsson, E., Wählby, C., and Lindblad, J. (2004). Robust Cell Image Segmentation Methods. Pattern Recognit. Image Anal. *14*, 157–167.

109. Wählby, C., Sintorn, I.M., Erlandsson, F., Borgefors, G., and Bengtsson, E. (2004). Combining intensity, edge and shape information for 2D and 3D segmentation of cell nuclei in tissue sections. J. Microsc. *215*, 67–76.

110. Nguyen, T.M., and Wu, Q.M.J. (2013). A Nonsymmetric Mixture Model for Unsupervised Image Segmentation. IEEE Trans. Cybern. *43*, 751–765.

111. Coelho, L.P. (2013). Mahotas: open source software for scriptable computer vision. J. Open Res. Softw. *1*, e3.

112. de Bruin, R.A.M., McDonald, W.H., Kalashnikova, T.I., Yates, J., and Wittenberg, C. (2004). Cln3 activates G1-specific transcription via phosphorylation of the SBF bound repressor Whi5. Cell *117*, 887–898.

113. The HDF Group. (2022). Hierarchical Data Format, version 5. https://www.loc.gov/preservation/digital/formats/fdd/fdd000229.shtml.

114. Collette, A. (2013). Python and HDF5: Unlocking Scientific Data (O'Reilly Media, Inc).

115. Ioffe, S., and Szegedy, C. (2015). Batch Normalization: Accelerating Deep Network Training by Reducing Internal Covariate Shift. Preprint at arXiv.

116. Hughes, M.E., Hogenesch, J.B., and Kornacker, K. (2009). JTK_CYCLE: an efficient non-parametric algorithm for detecting rhythmic components in genome-scale datasets. J. Biol. Rhythms *25*, 372–380.

117. Van Der Maaten, L., and Hinton, G. (2008). Visualizing Data using t-SNE. J. Mach. Learn. Res. *9*, 2579–2605.

118. Pedregosa, F., Varoquaux, G., Gramfort, A., Michel, V., Thirion, B., Grisel, O., Blondel, M., Prettenhofer, P., Weiss, R., Dubourg, V., et al. (2011). Scikit-learn: Machine Learning in Python. J. Mach. Learn. Res. *12*, 2825–2830.

119. Breeden, L.L. (1997). α-Factor synchronization of budding yeast. Methods Enzymol. *283*, 332–341.

120. Couvillion, M.T., and Churchman, L.S. (2017). Mitochondrial Ribosome (Mitoribosome) Profiling for Monitoring Mitochondrial Translation In Vivo. Curr. Protoc. Mol. Biol. *119*, 4.28.1–4.28.25.

121. Ingolia, N.T. (2010). Genome-wide translational profiling by ribosome footprinting. Methods Enzymol. *470*, 119–142.

122. Couvillion, M.T., Soto, I.C., Shipkovenska, G., and Churchman, L.S. (2016). Synchronized mitochondrial and cytosolic translation programs. Nature *533*, 499–503.

123. Wittke, S., Lewke, N., Müller, S., and Johnsson, N. (1999). Probing the molecular environment of membrane proteins in vivo. Mol. Biol. Cell *10*, 2519–2530.

124. Cherry, J.M., Hong, E.L., Amundsen, C., Balakrishnan, R., Binkley, G., Chan, E.T., Christie, K.R., Costanzo, M.C., Dwight, S.S., Engel, S.R., et al. (2012). Saccharomyces Genome Database: the genomics resource of budding yeast. Nucleic Acids Res. *40*, D700–D705.

125. Babicki, S., Arndt, D., Marcu, A., Liang, Y., Grant, J.R., Maciejewski, A., and Wishart, D.S. (2016). Heatmapper: web-enabled heat mapping for all. Nucleic Acids Res. *44*, W147–W153.

126. Wittenberg, C., Sugimoto, K., and Reed, S.I. (1990). G1-specific cyclins of S. cerevisiae: Cell cycle periodicity, regulation by mating pheromone, and association with the p34CDC28 protein kinase. Cell *62*, 225–237.

127. Tyers, M., Tokiwa, G., and Futcher, B. (1993). Comparison of the Saccharomyces cerevisiae G1 cyclins: Cln3 may be an upstream activator of Cln1, Cln2 and other cyclins. EMBO J. *12*, 1955–1968.

128. Deshaies, R.J. (1997). Phosphorylation and proteolysis: Partners in the regulation of cell division in budding yeast. Curr. Opin. Genet. Dev. *7*, 7–16.

129. Flory, M.R., Lee, H., Bonneau, R., Mallick, P., Serikawa, K., Morris, D.R., and Aebersold, R. (2006). Quantitative proteomic analysis of the budding yeast cell cycle using acid-cleavable isotope-coded affinity tag reagents. Proteomics *6*, 6146–6157.

130. Muzi Falconi, M.M., Piseri, A., Ferrari, M., Lucchini, G., Plevani, P., and Foiani, M. (1993). De novo synthesis of budding yeast DNA polymerase alpha and POL1 transcription at the G1/S boundary are not required for entrance into S phase. Proc. Natl. Acad. Sci. USA *90*, 10519–10523.

131. Ruxton, G.D. (2006). The unequal variance t-test is an underused alternative to Student's t-test and the Mann–Whitney U test. Behav. Ecol. *17*, 688–690.

132. Baryshnikova, A., Costanzo, M., Kim, Y., Ding, H., Koh, J., Toufighi, K., Youn, J.Y., Ou, J., San Luis, B.J., Bandyopadhyay, S., et al. (2010). Quantitative analysis of fitness and genetic interactions in yeast on a genome scale. Nat. Methods *7*, 1017–1024.

133. Wood, P.J., and Fulcher, R.G. (1984). Specific interaction of aniline blue with (1 → 3)-β-d-glucan. Carbohydr. Polym. *4*, 49–72.

STAR★METHODS

KEY RESOURCES TABLE

REAGENT or RESOURCE	SOURCE	IDENTIFIER
Chemicals, peptides, and recombinant proteins		
Hygromycin B	Wisent	400-141-UG
Nourseothricin	Jena Bioscience	96736-11-7
Ampicillin Sodium Salt	Fisher BioReagents	BP1760-25
Proteinase K	ThermoFisher	EO0491
FM™ 4-64 Dye	ThermoFisher	T13320
α-Factor Mating Pheromone, yeast	GenScript	RP01002
SUPERase•In™ RNase Inhibitor	Invitrogen	AM2696
SuperScript™ III Reverse Transcriptase	Invitrogen	18080-093
T4 Polynucleotide Kinase	NEB	M0201S
T4 RNA Ligase Reaction Buffer	NEB	B0216L
Phusion® High-Fidelity DNA Polymerase	NEB	M0530L
5X Phusion HF Buffer	ThermoFisher	F518L
CircLigase™	Epicentre	CL4111K
Aniline Blue solution	Sigma-Aldrich	B8563
Caspofungin diacetate	Sigma-Aldrich	SML0425
Tunicamycin from Streptomyces sp.	Sigma-Aldrich	T7765
Critical commercial assays		
Ribo-Zero Gold rRNA (Yeast)	Illumina	MRZY1306
Deposited data		
Cell cycle-resolved datasets and microscopy images	This study	thecellvision.org/cellcycle
Code for cell cycle and localization network training, single cell segmentation, and evaluation steps	This study	https://github.com/BooneAndrewsLab/CycleNET
Sequencing data	This study	GEO: GSE240513
Experimental models: Organisms/strains		
S. cerevisiae: Yeast GFP collection	Huh et al.[23]	N/A
S. cerevisiae: Cell cycle query strain	Kraus et al.[24]	N/A
S. cerevisiae: Imaging strains; Genotype: MATa XXX-GFP::HIS3 CAN1pr::TDH3pr-E2Crimson::HPH::can1Δ::STE2pr-LEU2 HTA2-mCherry::CaURA3 CDC11-TagRFP:: natMX lyp1Δ ura3Δ0 his3Δ1 leu2Δ0 met15Δ0	This study	N/A
S. cerevisiae: Sequencing strain; Genotype: MATa DAD2-GFP::HIS3 CAN1pr::TDH3pr-E2Crimson::HPH::can1Δ::STE2pr-LEU2 HTA2-mCherry::CaURA3 CDC11-TagRFP::natMX lyp1Δ ura3Δ0 his3Δ1 leu2Δ0 met15Δ0)	This study	N/A
S. cerevisiae: 6578; Genotype: MATα can1pr::TDH3pr-E2Crimson::HPH::can1Δ::STE2pr-LEU2 CDC11-TagRFP::natMX HTA2-mCherry::kanMX YMR295C-GFP(S65T)–His3MX lyp1Δ his3Δ1 leu2Δ0 ura3Δ0 met15Δ0	This study	N/A
S. cerevisiae: rho1-503 (ts)	Costanzo et al.[88]	N/A
S. cerevisiae: gsc2Δ0	Costanzo et al.[88]	N/A
S. cerevisiae: ygr273cΔ0	Costanzo et al.[88]	N/A

(*Continued on next page*)

Continued

REAGENT or RESOURCE	SOURCE	IDENTIFIER
S. cerevisiae: fks1Δ0	Costanzo et al.[88]	N/A
S. cerevisiae: ymr295cΔ0	Costanzo et al.[88]	N/A
S. cerevisiae: ura3Δ0 (control)	Costanzo et al.[88]	N/A
S. cerevisiae: BY4741	Brachmann et al.[101]	N/A
S. cerevisiae: ymr295cΔ	Giaever et al.[102]	N/A
S. cerevisiae: Strain JD 47	Dünkler et al.[103]	N/A
Software and algorithms		
Python 2.7	Python Software Foundation	N/A
Tensorflow v1.6.0	tensorflow.org	N/A
R 4.1	R Core Team	N/A
Bioconductor v3.13	Bioconductor	N/A
Prism	GraphPad	N/A
Excel	Microsoft 365	N/A
Adobe Illustrator 27.0.1	Adobe	N/A
Gephi 0.9.2	Gephi.org	N/A
ImageJ	Schneider et al.[104]	http://imagej.org

RESOURCE AVAILABILITY

Lead contact

Further information and requests for resources and reagents should be directed to and will be fulfilled by the Lead Contact, Brenda Andrews (brenda.andrews@utoronto.ca).

Materials availability

This study did not generate new unique reagents.

Data and code availability

- All sequencing data are deposited in Gene Expression Omnibus (accession number GSE240513) and are publicly available as of the date of publication. All protein-specific cell cycle results are available at https://thecellvision.org/cellcycle. Data and additional files that support the analyses are available at https://thecellvision.org/cellcycle/supplemental. Microscopy images are available for browsing at https://thecellvision.org/cellcycle.
- Code for the cell cycle and localization network training, single cell segmentation, and evaluation steps is publicly available as of the date of publication at https://github.com/BooneAndrewsLab/CycleNET.
- Any additional information required to reanalyze the data reported in this paper is available from the lead contact upon request.

EXPERIMENTAL MODEL AND STUDY PARTICIPANT DETAILS

All experiments were conducted using genetically modified strains of the single celled budding yeast, *Saccharomyces cerevisiae*. Genotypes and growth conditions are provided below.

Yeast Strains for Microscopy Experiments

In total, ~3900 strains were imaged for the purposes of quantifying fcell cycle-specific changes in protein abundance and localization. These strains were generated using SGA technology[28] to cross a fluorescent query strain with cell cycle positional markers into the ORF-GFP Fusion Collection. The resultant strains were of the following genotype:

MATa XXX-GFP::HIS3 CAN1pr::TDH3pr-E2Crimson::HPH::can1Δ::STE2pr-LEU2 HTA2-mCherry::CaURA3 CDC11-TagRFP::natMX lyp1Δ ura3Δ0 his3Δ1 leu2Δ0 met15Δ0

Haploid *MAT*a strains were inoculated into synthetic medium with 1mM methionine, 100 μg/mL NAT, 300 μg/mL Hygromycin B, and 2% glucose. Cultures were grown to saturation in 96-well microplates (200 μL volume) with glass beads at 30°C. Cultures were diluted in 600 μl low fluorescence synthetic medium containing 5 g/L ammonium sulfate, 1mM methionine, 20 μg/mL ampicillin, and 2% glucose, in deep well blocks with glass beads. Cultures were grown to early log phase at 25°C and then transferred to 384-well glass-bottom imaging plates (CellCarrier, Perkin Elmer) using a liquid handling robot (S&P Robotics). Strains were imaged at room temperature (RT).

Yeast Strains for Sequencing Experiments

The strain used for gene expression and translational efficiency measurements contained the three fluorescent cell cycle positional markers from our microscopy query strain as well as a marker of the spindle pole bodies and mitotic spindle fused to GFP from the ORF-GFP Fusion Collection. The resultant strain had the following genotype:

MATa DAD2-GFP::HIS3 CAN1pr::TDH3pr-E2Crimson::HPH::can1Δ::STE2pr-LEU2 HTA2-mCherry::CaURA3 CDC11-TagRFP::natMX lyp1Δ ura3Δ0 his3Δ1 leu2Δ0 met15Δ0

Cells were grown overnight at 25°C in YEPD to saturation and then diluted to OD_{600} ~0.013 in 2 L YEPD and allowed to grow for another ~16 hours until reaching OD_{600} ~0.1-0.3. α-factor was added at a concentration of 5 μg/ml and cells were allowed to grow at 30°C for 1.5 doublings. Cells were filtered onto nitrocellulose membranes and re-suspended in cold YEPD for two wash cycles before being re-suspended in RT YEPD to OD_{600}~0.4. Cells were shaken in 3x2 L flasks at 30°C as samples were collected.

Yeast Strains for *YMR295C* characterization

Single-knockout strains used were of the following genotype[88]:

MATα ORFΔ0::natMX4 can1Δ0::STE2pr-Sp_HIS5 lyp1Δ0 his3Δ1 leu2Δ0 ura3Δ0 met15Δ0 LYS2+

The strain carrying the temperature sensitive (ts) allele of the *RHO1* gene was of the following genotype[88]:

MATα rho1-503::NatR can1Δ::STE2pr-Sp_HIS5 lyp1Δ0 his3Δ1 Leu2Δ0 ura3Δ0 met15Δ0

Double-knockout mutants were generated via standard SGA procedures[28] by crossing the *ymr295c*Δ strain from yeast knockout collection[102] (genotype: *MATa ymr295cΔ0::kanMX4 his3Δ1 leu2Δ0 ura3Δ0 met15Δ0*) with all the single-knockout and ts strains, as well as with a wild type control strain (*MATa ura3Δ0::natMX4 can1Δ0::STE2pr-Sp_HIS5 lyp1Δ0 his3Δ1 leu2Δ0 ura3Δ0 met15Δ0 LYS2+*).

For the experiments involving *YMR295C* overexpression for Aniline Blue staining, the wild type BY4741 strain[101] was used. To examine Ymr295c-GFP localization upon overexpression, strain 6578 of the following genotype was used:

MATα can1pr::TDH3pr-E2Crimson::HPH::can1Δ::STE2pr-LEU2 CDC11-TagRFP::natMX HTA2-mCherry::kanMX YMR295C-GFP(S65T)–His3MX lyp1Δ his3Δ1 leu2Δ0 ura3Δ0 met15Δ0

Strains used for the split-ubiquitin experiments and their construction are described in the respective section (split-ubiquitin assay).

METHOD DETAILS

Cell cycle proteomics

Yeast Strain and Array Construction

Construction of the fluorescent, cell cycle-specific query strain has been previously described[24] and has the following genotype: *MATα CAN1pr::TDH3pr-E2Crimson::HPH::can1Δ::STE2pr-LEU2 HTA2-mCherry::CaURA3 CDC11-TagRFP::natMX lyp1Δ ura3Δ0 his3Δ1 leu2Δ0 met15Δ0*. Briefly, the query strain expresses fluorescent markers of the cytoplasm (*TDH3*pr::E2Crimson), nucleus (*HTA2*-mCherry), and the septin (*CDC11*-TagRFP), which facilitate automated classification of cell cycle stage (see below).

Synthetic Genetic array (SGA) analysis was performed as described[28] with minor modifications. Our cell cycle-specific query strain was marked with *natMX*, *HPH*, and *CaURA3*, as well as the *MAT*a-specific promoter (*STE2pr*) driving expression of *LEU2*. This query strain was crossed to the ORF-GFP Fusion Collection[23] using 384-format replica pinning on a Virtek Colony Arrayer (Biorad Laboratories). As previously described,[28] successive pinning onto selective media was used to ultimately selecting for *MAT*a haploid cells containing our fluorescent cell cycle positional markers as well as unique GFP-fusion proteins from the ORF-GFP Fusion Collection.[23]

Yeast cells were transferred from solid media into 96-format microplates by hand-pinning. Each well contained a 3mm glass bead and was filled with 200μL liquid synthetic dextrose (SD) medium. Cultures were grown overnight to saturation (OD_{600} ~12) in a shaking incubator at 25°C. Saturated cultures were inoculated to early log phase in liquid low fluorescence (LF) medium[105] and grown for 18-20 hours at 25°C to a final OD ~0.2. Cultures were transferred to 384-well glass-bottom imaging plates (PerkinElmer, Part No. 6057300) and centrifuged at 500 rpm for 30 seconds to prepare cells for immediate imaging.

Live-Cell Image Acquisition

High-throughput imaging was performed using the Perkin Elmer, QEHS Evotec Opera™, a spinning disk confocal microscope for automated image acquisition. Ten images were acquired in each well, imaging at 60X magnification (water immersion, NA=1.2) through a single z-axis plane. Simultaneous 800 ms excitations from 488, 561 and 640 nm lasers were used to visualize GFP, RFP, and F-RFP fluorescence respectively. Fluorescence was captured separately using a 520/30 nm band-pass (BP) filter for GFP, 585/20 nm BP for RFP, and 690/70 nm BP for F-RFP, along with a 568 nm detection dichroic mirror, and a 405/488/561/640 nm quadruple BP primary dichroic mirror. Images were saved as 16-bit proprietary .tiff (".flex") files.

Image Post-Processing

To characterize each cell in our High Content Screening (HCS) datasets, we developed a segmentation technique based on the seeded watershed algorithm.[106–108] The watershed algorithm can be interpreted by treating gray-scale pixel intensities as a topological map, where boundaries are determined by dimmer ''catchment basins'' between higher intensity regions. Using every local maxima as a seed region for the algorithm almost always results in over-segmentation. An alternative is to explicitly define seed regions to

initialize the algorithm. As our HCS screens almost always contain nuclear and cytoplasmic markers, an intuitive approach is to define nuclear regions as seeds and use region growing techniques to define cellular boundaries.[108,109]

Next, instead of relying on thresholding techniques, we implemented a non-symmetric mixture model (NSMM) composed of multiple Student's t-distributions to classify pixels as belonging to background, cytoplasmic, or nuclear regions.[110] In this model, each component is modeled with multiple Student's t-distributions. We briefly outline the algorithm below:

The probability of pixel x_i given component j is defined by a mixture of K_j distributions,

where K_j is the number of distributions used to model component j with parameters Ω_j

$$p(x_i|\Omega_j) = \pi_{ij}\sum_{k=1}^{K_j}\eta_{jk}S(x_i|\mu_{jk},\Sigma_{jk},\upsilon_{jk})$$

where $S(x_i|\mu_{jk},\Sigma_{jk},\upsilon_{jk})$ is the Student's t $-$ distribution given by:

$$S(x_i|\mu_{jk},\Sigma_{jk},\upsilon_{jk}) = \left(\frac{\Gamma(\upsilon_{jk}/2+D/2)|\Sigma_{jk}|^{-1/2}}{(\upsilon_{jk}\pi)^{D/2}\Gamma(\upsilon_{jk}/2)}\right)\times\frac{1}{\left[1+\upsilon_{jk}{}^{-1}(x_i-\mu_{jk})^T\Sigma_{jk}{}^{-1}(x_i-\mu_{jk})\right]^{(\upsilon_{jk}+D)/2}}$$

where D is the dimensionality $(D = 1$ for grayscale images$)$, μ_{jk}, Σ_{jk}, and υ_{jk} are the mean, covariance, and degrees of freedom, respectively. $\Gamma(\cdot)$ is the Gamma function defined by:

$$\Gamma(\mathrm{n}) = \int_0^\infty t^{n-1}e^{-t}dt$$

and the prior probability distribution π_{ij} is given by:

$$\pi_{ij} = \frac{exp\left(\frac{\beta}{N_i}\sum_{m\epsilon\partial_i}z_{mj}^{(t-1)}\right)}{\sum_{k=1}^{K}exp\left(\frac{\beta}{N_i}\sum_{m\epsilon\partial_i}z_{mk}^{(t-1)}\right)}$$

where $z_{mj}^{(t-1)}$ represents the posterior probability of the m pixels in the neighbourhood of pixel i $(m\epsilon\partial_i)$ at iteration $t-1$ and N_i represents the number of neighbouring pixels.

The parameters in the model were updated using the expectation-maximization algorithm as described in detail in Nguyen and Wu.[110] Once nuclear and cytoplasmic regions were identified, the seeded watershed algorithm implementation in the Mahotas computer vision library for Python[111] was used to determine the final boundaries between cells. A pixel-level ground truth dataset was not available to quantify the accuracy of the algorithm. Instead, we validated the performance of the algorithm on 185 test images sampled from a variety of experimental plates. Source code for this segmentation technique and datasets of segmented cells are provided in https://github.com/BooneAndrewsLab/CycleNET.

In silico synchronization using CycleNET

To circumvent the biological artifacts and logistical experimental hurdles associated with high-throughput synchronization of yeast cells for cell cycle analyses, we developed CycleNET a classification scheme for in silico synchrony of single cell images of asynchronous yeast cultures. We used a number of metrics to identify cells at different cell cycle stages, that we could then use as a training

set. First, cell size information was calculated from cytosolic pixel measurements and used to distinguish images of early (Pre-START) and late (Post-START) G1 cells. To account for asymmetric cell division between mother and daughter cells, in each cell population only the smallest 25% of cells were classified as Pre-START, while the largest 25% were classified as Post-START. We validated this classification approach by imaging strains that contained a Whi5-GFP fusion protein; Whi5 is a well-established indicator of cell cycle START, and localizes to the nucleus in early G1 and the cytoplasm after START initiation.[35,112] Quantification of nuclear:cytoplasmic GFP intensity revealed that using cell size quartiles was an effective approach for accurately distinguishing images of early and late G1 cells (Figure S1B).

Next, we used the appearance of a bud to distinguish Post-START G1 cells from those undergoing DNA replication. Bud size information was calculated by counting cytosolic pixels, and the fluorescent septin marker in the query strain allowed separate quantification of mother and bud parameters following computational cell segmentation. We also used bud size information to distinguish cells in S/G2 from those that had entered Mitosis by determining a size threshold based around spindle pole body dynamics. We imaged a strain containing a Dad2-GFP fusion protein which allows for visualization of mitotic spindle dynamics so that we could visually distinguish Pre- and Post-Mitotic cells, sort them, and then calculate their relative bud sizes (Figure S1C). This information was used for prediction of the respective cell cycle phases without Dad2-GFP. Finally, we used nuclear dynamics to distinguish the three major phases of Mitosis: Metaphase, Anaphase, and Telophase.

Training and test datasets for machine learning were created by cropping single cells using a 64x64 pixel window centered on the cells. In some cases, cells were resized to fit in the window and pixel intensities belonging to cells bordering the current cell object were replaced with intensity values sampled from the background class intensity distribution. We generated cell cycle labels for the dataset by manually labeling each cell into one of six cell cycle stages and three additional categories covering dead cells, non-cellular objects, and cells that had been improperly segmented. In total we labeled 12,717 single cells and used 90% of the data (11,445 cells) to train CycleNet and used the remaining 10% (1,272 cells) to evaluate the model's classification performance. Images of cropped single cells were stored as row vectors or tensors in HDF5 datasets[113] using the h5py library for Python.[114]

We used the code-base released with DeepLoc[24] to train CycleNET with a different neural network architecture. The architecture consisted of three convolutional and pooling layers followed by two fully connected layers. The numbers of feature maps in the convolutional layers were 32, 64, and 64. Max pooling was applied with a window size of 2 and stride of 2 after convolutional layers 1, 2, and 3. Following the third pooling layer, activations in the feature maps were flattened into a vector and subsequent layers were fully connected. We used two fully connected layers with 1024 and 9 features. We applied batch normalization[115] at every layer prior to applying the rectified linear unit activation function. The last layer represents the cell cycle classes in the trainings set. We applied the softmax function to the activations of the final output layer to produce a distribution over the cell cycle classes. Code for training this network and pretrained models are provided in https://github.com/BooneAndrewsLab/CycleNET.

Evaluating CycleNET Performance

We used the held-out test set consisting of ~10% of the labeled data (1,272 cells) to evaluate the model's classification performance by computing classification accuracy across different classes. The resulting confusion matrix is shown in Figure 1C. The overall training set accuracy was 94.7% while the test set accuracy was 93.8%. Most misclassified samples were Metaphase cells misclassified as S/G2 and over_segmented cells misclassified as Late_G1 (over_segmented cells are mis-segmented cells in which budding cells are segmented as two separate cells).

Quantifying Protein Concentration

We extracted the mean intensity by area within each cell based on the segmentation algorithm mentioned above. For each protein we computed the mean concentration (I_g) across the population, binned by cell cycle.

Scoring Periodicity for Protein Concentration Measurements

We adopted the approach used in Kelliher et al.[12] to evaluate periodicity in our dataset. Implementations of the four periodicity algorithms (de Lichtenberg (DL),[32] LS,[30,31] JTK_CYCLE (JTK),[116] and persistent homology (PH)[33] described in Deckard et al.[29] were provided by Francis Motta. In brief, de Lichtenberg is a permutation-based approach, which combines a regulation-based score with a periodicity score. JTK_CYCLE correlates pairs of points and computes the significance of the correlation in relation to a reference curve. Persistent homology examines persistence pairings of minima and maxima along the curve, with the ideal oscillation consisting of a single minima and maxima. Lomb-Scargle is a Fourier style method developed to deal with irregular data sampling rates. The implementations are written in *R* and contain a Python wrapper to run all four algorithms on data stored in text files. We used the implementations to score the normalized RNA sequencing, ribosome profiling, and HCS concentration datasets. These datasets were normalized by computing the $\log_2$ transform of the raw data divided by the mean value for each transcript or protein. They were further normalized by subtracting the mean expression or abundance across all conditions for the different cell cycle stages. Ranked hit-lists for each dataset were generated by adding up the rankings from the four algorithms for each transcript or protein. We used manual data inspection to determine a cut-off for periodic concentration by examining visualized cell cycle profiles for presence of sinusoidal dynamics and their standard deviations using the sparkline function in Microsoft Excel, and filtered these data further to remove false positives, and proteins with fluorescence at the GFP channel less than that of cellular autofluorescence, ultimately identifying 810 proteins that change in concentration with cell cycle progression (Table S1).

Peaks and Troughs of protein dynamics

The cell cycle phases where each protein had its maximum and minimum concentration and total abundance were estimated on the basis of mean concentration and abundance, respectively, at each cell cycle phase across all three biological replicates. If after

correction for cellular autofluorescence the maximum of the replicate men was below zero, but above zero in two out of three replicates, then the replicate with the highest maximum value was used for determination of the peak cell cycle phase. If the autofluorescence-corrected replicate-mean minimum was negative, the trough was determined on the basis of the replicate with the lowest minimum value above the detection limit.

Quantitative Analyses of Protein Concentration Data

For quantitative analyses of protein concentration data, we corrected for background autofluorescence by subtracting the mean cellular autofluorescence of GFP-free cells at each cell cycle phase from the measured mean GFP fluorescence for each protein. To increase our quantitative accuracy, unless indicated otherwise, we restricted the determination of absolute protein-specific concentration changes to proteins with a minimum cell cycle level value $\geq$5% of that of cellular autofluorescence at each replicate. The same holds true for determination of changes in total protein abundance. For the 161 measured RPs, we excluded from quantitative analyses twelve RPs that had an unexpected localization at the nucleus and/or the nucleolus, along with six RPs which had below or close to detection limit levels.

Protein Abundance Scaling with Cell Size During G1

A protein was classified as having positive or negative differential scaling with cell size if its concentration during G1 consistently increased or decreased, respectively, in all three replicates. Proteins with inconsistent increase or decrease in their concentration across replicates were classified as having no differential scaling with cell size.

Training DeepLoc

Training and test datasets for machine learning were created by cropping single cells using a 64x64 pixel window centered on the cells. We generated localization labels for a training dataset by manually labeling cells into one of 22 localization classes. We developed an efficient labeling method that initially annotates cells based on their known protein localization and then allows filtering of cells that are mislabeled by selecting them from a grid. In total we labeled 18,129 single cells and used 90% of the data (16,305 cells) to train DeepLoc[24] and used the remaining 10% (1,824 cells) to evaluate the model's classification performance.

We used the code-base released with DeepLoc[24] to train DeepLoc on this dataset. The numbers of feature maps in the convolutional layers were 64, 64, 128, 128, 256, 256, 256, and 256. Max pooling was applied with a window size of 2 and stride of 2 after convolutional layers 2, 4, and 8. Following the third pooling layer, activations in the feature maps were flattened into a vector and subsequent layers were fully connected. We used three fully connected layers with 512, 512, and 22 features. We applied batch normalization[115] at every layer prior to applying the rectified linear unit activation function. The last layer represents the localization classes in the trainings set. We applied the softmax function to the activations of the final output layer to produce a distribution over the localization classes.

We used the held-out test set consisting of ~10% of the labeled data (1,824 cells) to evaluate the model's classification performance by computing classification accuracy across different classes. The resulting confusion matrix is shown in Figure S1D. The overall training set accuracy was 87.0% while the test set accuracy was 83.7%. Most misclassified samples were confusions between similar classes like Vacuole with Vacuole Periphery and Bud with Bud Periphery.

Scoring Periodicity for Protein Localization Measurements

We used the same approach used to score the periodicity of protein abundance measurements (adopted from Kelliher et al.[12]) to evaluate periodicity in protein localization changes. After filtering any strains for which there were less than 10 cells in any of the six cell cycle phases, we ran each scoring metric on localization vectors for each protein and cell cycle stage individually to see in which compartments proteins might be periodically moving. The dataset was normalized by subtracting the mean localization vector across all conditions for the different cell cycle stages. Ranked hit-lists were generated by adding up the rankings from the four algorithms for each protein and each localization class. We used manual data inspection to determine a cut-off for periodic movement and, after filtering these data further to remove false positives reflective of network errors or protein expression changes rather than localization movements, we were left with a high-confidence list of 405 periodic proteins (Table S1).

To calculate the mean correlation among members of the same protein complex, the R values of the localization profiles of each possible protein pair in our hit list were first transformed using a Fisher Z transformation. Then, z-values of proteins of the same complex were averaged and the average was converted back to an R value. Members of each protein-complex were identified using the protein complex standard from Costanzo et al.[88] Then, for the random calculation, three ORFs were randomly sampled from the correlation matrix and the above steps were applied to get the complex R value.

Flux Networks and Summary Statistics

For downstream analyses involving protein localization changes following periodicity scoring, the Deeploc activation scores for localization classes Bud and Bud Periphery, and classes Vacuole and Vacuole Periphery, were added up to the single combined classes Bud / Periphery, and Vacuole / Periphery, respectively, as these were the classes where misclassification was occasionally observed (Figure S1D), and the class None was removed. To minimize false-positive cases, unless indicated otherwise, we introduced an additional criterion for including an identified periodic protein to summary statistics and flux networks. Specifically, we required that a protein with periodic localization displayed both an increase in localization at a certain class ($\geq$ 0.1 DeepLoc activation), and a parallel decrease at another ($\geq$ 0.1 DeepLoc activation) during the same cell cycle phase transition. A change of $\geq$ 0.1 in DeepLoc activation in a localization class for significantly periodic proteins was also required for inclusion of a protein in the enrichment analysis presented in Figure 2D. For the flux network depicting both changes in protein concentration and localization (Figures 5F–5I), periodic proteins were also required to display a minimum of 10% change in concentration. The flux network showing cell cycle-specific

protein movements between localization classes was generated using Gephi (0.9.2) and Adobe Illustrator, while the network depicting changes in both localization and concentration was generated using Gephi (0.9.2), Excel, and Adobe Illustrator.

Compartment Connectivity Score

The compartment connectivity score was calculated by first identifying the cases of protein movement within any two localization classes ($\geq$ 0.1 increase in DeepLoc activation in one class and parallel $\geq$ 0.1 decrease in another for the same protein) at each major cell cycle transition (Early to Late G1, Late G1 to Early Mitosis, Early to Late Mitosis, Late Mitosis to Early G1) for any of the proteins the we identified as periodic in terms of localization. Then, all cases of protein movement at all transitions were summed for each two localization classes. Finally, the total number of cases within a localization class with another, was normalized for the total number of cases between this class and all other localization classes. Connectivity score was not calculated for Cytoplasmic Foci and Eisosomes, due to the low number of total cases (two and three, respectively) involving these two classes. For visualization, data were clustered before normalization using Cluster 3.0 (hierarchical, average linkage), and were subsequently normalized as described above.

Comparison of dynamics among different datasets

Gene groups with similar transcript and protein concentration dynamics (Figures 4B–4D) were identified by hierarchical clustering of transcript level and protein concentration data. Six genes clustered in a group that could not be readily attributed to any of the three main categories. For genes with significant periodicity in all three datasets (protein concentration, transcript level, translational efficiency) displayed in Figure 4E, normalized effect was computed by averaging the values at each cell cycle phase across all replicates and normalizing the resulting cell cycle signal from 0 (min, blue) to 1 (max, yellow).

t-SNEs

To generate the data visualization in Figure S1E, we applied the t-Distributed Stochastic Neighbor Embedding (t-SNE)[117] to the cell cycle-specific localization vectors generated by DeepLoc for each protein, and to the background-corrected cell cycle-specific protein concentration measurements, all scaled between 0 and 1. We used the t-SNE implementation from the scikit-learn library.[118] Here, we set the perplexity value to 30, and the metric to "cosine". The genes were colored according to their biological process annotations, as given by Costanzo et al.[88] in their Supplementary Data File 5.

Growth Rate Measurements

For growth rate measurement of cytosolic RP-GFP fusion strains, we grew the strains from the GFP collection[23] on YEPD plates together with non-RP control strains (WT (4 x colonies), *WHI5*-GFP (3 x colonies), and *ALD6*-GFP (3 x colonies)). The strains were then transferred to beaded 96-well microplates containing 150 μl YEPD medium per well and were incubated at RT with rotation for eight hours. Cultures were then diluted in the evening into deep 96-well blocks containing 600 μl YEPD per well and incubated overnight at RT with rotation. Cultures were then diluted to an OD_{600} ~0.1 in 200 μl YEPD in 96-well microplates in triplicate. Growth was monitored via a microplate reader (Tecan Sunrise™) at 29°C with 30-minute sampling intervals. For analysis, the linear part of the log-transformed growth curve was used to estimate doubling time from which the growth rate of each strain was determined.

FM™ 4-64 Staining

For FM™ 4-64 (Thermo Fisher) staining, 1 mL of log-phase cells (LF SD + leucine, methionine, uracil (LMU)) medium at RT) was transferred to an Eppendorf tube and centrifuged at 5000 x g for 5 min at RT. The cell pellet was resuspended in 50 μL YEPD + 1 μL FM™ 4-64 (1.6 mM stock in DMSO). Cells were incubated in a 30̊C water bath for 20 min and 1 mL YEPD was added. Cells were centrifuged at 5000 x g for 5 min at RT and the cell pellet was resuspended in 1 mL YEPD, and cells were transferred to a culture tube containing 4 mL of YEPD, then incubated with shaking at 30̊C for 3h. The culture (5 mL) was centrifuged for 5 min at 3000 x g at RT, resuspended in 1 mL sterile water, centrifuged again at 5000 x g for 5 min at RT, and then the pellet was resuspended in 25 μL LF SD + LMU. Cells were imaged with an Opera Phenix (Perkin Elmer) confocal microscope, using a 63x (water immersion, NA=1.15) objective (FM™ 4-64: excitation 488 nm, emission 650-760 nm; GFP: excitation 488 nm, emission 500-550 nm).

Cell cycle gene expression & translational efficiency

Sample Collection

For the purpose of manually assessing cell synchrony, we crossed our fluorescent, cell cycle-specific query strain to a strain containing *DAD2-GFP::HIS3*, allowing us to visualize cell cycle transitions based on spindle and spindle pole body dynamics rather than using bud size thresholds. Cells were grown overnight at 25°C in YEPD to saturation and then diluted to OD_{600} ~0.013 in 2 L YEPD and allowed to grow for another ~16 hours until reaching OD_{600} ~0.1-0.3. Yeast cells were arrested in α-factor using standard protocols.[119] Briefly, α-factor was added at a concentration of 5 μg/mL and cells were allowed to grow at 30°C for 1.5 doublings. Shmoo-ing morphology was confirmed using light microscopy prior to washing. Cells were filtered onto nitrocellulose membranes and re-suspended in cold YEPD for two wash cycles before being re-suspended in RT YEPD to OD_{600}~0.4. Cells were shaken in 3x2 L flasks at 30°C. At 10-minute intervals, 250 mL of cells were filtered onto nitrocellulose membranes and flash frozen on membranes in 15 mL falcon tubes. Concurrently, ~40 μL cells were pipetted into a single well in a 384-well Cell Carrier Ultra plate (Perkin Elmer Part No. 6057300), spun down at ~500 rpm for 30 seconds and imaged on the Opera Phenix using the same parameters outlined above. Samples were collected for 2 hours on two separate occasions, producing 2x13 sample replicates. Using manual image inspection, we quantified the fraction of cells in each of the six cell cycle stages used during our proteomics assays, and selected the five samples in each replicate that demonstrated the greatest synchrony to each of these stages (excluding G1 Pre-START).

Harvesting Samples

Cells were harvested and lysed according to Couvillion and Churchman[120] except that cells were frozen directly on nitrocellulose membranes. Briefly, frozen cells on nitrocellulose membranes were placed in metal casings with frozen lysis buffer to a total of 4 g. Samples were harvested four at a time by placing two casings containing separate samples in a mixer mill and grinding for 3 minutes at 15 Hz, while two other casings were submerged in liquid nitrogen. Casings were swapped for six rounds of grinding, after which samples were scraped into 50 mL eppendorf tubes with a pre-chilled spatula. Lysates were pre-cleared by spinning at 3000xg for 5 minutes at 4oC, supernatant was transferred to a fresh eppendorf tube and then cleared by spinning at 20,000xg for 10 minutes at 4°C. Samples were distributed into 250 μL aliquots and flash frozen in liquid nitrogen.

RNA Sequencing

RNA sequencing was performed according to Couvillion and Churchman[120] using a single 250 μL aliquot of cleared lysate for each cell cycle time-point.

First, lysate was brought to 390 μL with 10 mM Tris, pH 7.0 and allowed to reach RT. 10 μL of 20% SDS were added, followed by 2 μL of 20 μg/mL proteinase K and a 20 minute incubation at 42°C. 40 μL of 3M sodium acetate were added, followed by a phenol chloroform extraction using 600 μL of 5:1 acid phenol:chloroform (pH 4.5) before being ethanol precipitated. Pellets were re-suspended in 40 μL of 10 mM Tris, pH 7.0.

Next, RNA was diluted 1:10 and quantified using NanoDrop. Based on NanoDrop readings, 50 μg of RNA were brought up to 25 μL total volume with 10 mM Tris, pH 7.0. This mixture was combined with 26 μL RNase-free water, 6 μL DNase buffer, and 3 μL RQ1 DNase and then incubated for 30 minutes at 37oC. Next, 240 μL of RNase-free water were added to this solution, followed by 300 μL of 5:1 acid phenol:chloroform (pH 4.5) for a phenol-chloroform extraction. Following this extraction, RNA was ethanol precipitated and then re-suspended in 31 μL 10 mM Tris, pH 7.0.

Next, RNA was diluted 1:10 and quantified using NanoDrop. Based on NanoDrop readings, 5 μg RNA were added to the Ribo-zero kit (Ribo-zero Gold, Illumina cat no. MRZY1306). Following rRNA depletion in accordance with Ribo-zero kit instructions, final sample volumes were brought to 200 μL with RNase-free water. Samples were ethanol precipitated and then re-suspended in 16 μL 10 mM Tris, pH 8.0.

Prior to RNA fragmentation, we performed a test using a single sample to determine the appropriate reaction time. To do this, 4 μL RNA was combined with 36 μL RNase-free water and 40 μL 2X alkaline hydrolysis buffer and then distributed into four PCR tubes with a volume of 20 μL in each tube. Tubes were incubated at 95°C for 0, 10, 20, or 30 minutes, after which samples were isopropanol precipitated. Pellets were re-suspended in 10 μL 1X urea loading buffer and then denatured for 90 seconds at 80°C followed by another 90 seconds on ice. Test samples were loaded into a 15% TBE-urea polyacrylamide gel that had been pre-run for 15 minutes at 200 V. Samples, along with a 10 base pair denatured ladder, were run at 200 V for 1 hour, after which the gel was stained with SYBR gold (3 μL in 30 mL TBE) for 3 minutes at RT. Next, the gel was rinsed with dH2O, placed in a plastic sheet –protector and visualized on the Typhoon fluorescent/phosphorescent image scanner (GE Healthcare Life Sciences) using the 488 nm laser, 520 nm emission filter. Fragmentation time was selected based on the time at which the majority of RNA fragments were found in the 30-70 nucleotide range.

Samples were fragmented using conditions determined during the fragmentation test, but with twice as much starting material. After visualizing fragmented samples on the Typhoon Scanner, they were rapid gel extracted using Costar Spin-X columns and then isopropanol precipitated. Pellets were re-suspended in 5 μL RNase-free water.

Samples were loaded into a thick (1.5 mm) 12% TBE-urea gel and run at 200 V for 1 hour. Samples were fast gel extracted, isopropanol precipitated and then re-suspended in 5 μL RNase-free water. Libraries were generated by performing dephosphorylation, 3' ligation, reverse transcription, and circularization reactions as described below.

Samples were denatured for 90 seconds at 80°C followed by 30 seconds on ice. Next, samples were combined with 0.95 μL 10X T4 PNK buffer (NEB), 1.0 μL T4 PNK (NEB cat no. M0201S), and 2.55 μL RNase-free water. Samples were placed at 37°C for 1 hour and then 70°C for 10 minutes.

Samples were combined with 0.5 μL of a 5' pre-adenylated, barcode random hexamer, 3' blocked linker and denatured for 90 seconds at 80°C followed by 30 seconds on ice. Next, samples were combined with 8 μL of 50% PEG, 1 μL of 10X T4 RNL2 buffer (NEB cat no. B0216L), and 1 μL T4 RNL2, tr (made in-house). The reaction was allowed to sit at RT for 3 hours, after which it was brought to 400 μL with 340 μL of RNase-free water, 40 μL NaOAc, and 0.5 μL LPA. Samples were isopropanol precipitated, then pellets were re-suspended in 10 μL 1X urea loading buffer, denatured, and then loaded into a 15% TBE-urea polyacrylamide gel that had been pre-run for 15 minutes at 200 V. Samples were run for 1 hour at 200 V, visualized, and then fast gel extracted and isopropanol precipitated as previously described.

RNA was re-suspended in 10 μL 10 mM Tris, pH 8.0 and combined with 1.25 μM oSMD-RT1 in PCR tubes. Samples were denatured as described above. Next, samples were combined with 4 μL 5X FS buffer, 1 μL 10 mM dNTPs, 1 μL 0.1 M DTT, 1 μL Superase·In (Invitrogen cat no AM2696), and 1 μL SuperScriptIII (Invitrogen cat no. 18080-093). The reaction was allowed to sit at 48°C for 30 minutes before being combined with 2.2 μL 1N NaOH and allowed to sit for another 20 minutes at 98°C. Next, samples were combined with 0.7 μL LPA, 157.1 μL ddH2O, and 20 μL 3M NaOAc. Samples were mixed and then isopropanol precipitated and resuspended in 10 μL 1X urea loading buffer, denatured, and then loaded into a 15% TBE-urea polyacrylamide gel that had been pre-run

for 15 minutes at 200 V. Samples were run for 1 hour at 200 V, visualized, and then fast gel extracted and isopropanol precipitated as previously described, but with the exception that samples were precipitated with 1/10 volume 3M NaCl and re-suspended in 5 μL RNase-free water.

Next, 5 μL of the cDNA sample were combined with 10 μL RNase-free water, 2 μL of 10X Circ ligase buffer (Epicentre cat no. CL4111K), 1 μL of 1 mM ATP, 1 μL of 50 mM MnCl2, and 1 μL of Circ ligase (Epicentre cat no. CL4111K). This mixture was incubated at 60°C for one hour, followed immediately by a 10-minute incubation at 80oC.

Prior to PCR amplification, we performed a test using 3 μL of each sample to determine the appropriate number of reaction cycles. To do this, 3 μL circular cDNA was combined with 10 μL of 5X Phusion buffer (HF) (Thermo Scientific™ cat no. F518L), 1 μL of 10 mM dNTPs, 0.9 μL of 20 μM reverse primer (oSMD2), 0.9 μL of 20 μM barcoded forward primer (oSMD1, oMTC1, oMTC2, etc.), 33.8 μL ddH2O, and 0.48 μL of Phusion (2 U/μL) (NEB cat no. M0530L). The mixture was divided equally into three separate PCR tubes (16.7 μL per tube) for each sample. PCR amplification proceeded by the following protocol: 98°C for 30 seconds, followed by 8, 10, or 12 temperature shifting cycles of 98°C for 30 seconds, 65°C for 15 seconds, and 72°C for 7 seconds.

Next, samples were run on an 8% non-denaturing polyacrylamide gel at 180V for 45 minutes and then visualized using the Typhoon Scanner (as described above). PCR cycle number was selected based on a trade-off between product band size and non-specific band size.

PCR reactions were repeated as above, but only with the optimal number of reaction cycles. Samples were run on gels and visualized as above, after which they were overnight gel extracted with 670 μL of 0.3 M NaCl, 1 mM EDTA, and 10 mM Tris, pH 8.0. Following gel extraction, samples were precipitated in 680 μL isopropanol and then re-suspended in 15 μL of 10 mM Tris, pH 8.5.

Final library concentration and quality of the samples were assessed using the Qubit Fluorometric Quantification system with high-sensitivity dsDNA kit, and Agilent Bioanalyzer with DNA high-sensitivity chip, according to manufacturer's instructions. Sequencing was performed on an Illumina NextSeq 500 system using the custom "Read 1" primer oNTI202 (Sequence: 5' CGACAGG TTCAGAGTTCTACAGTCCGACGATC 3').

Ribosome Profiling

Ribosome profiling was performed according to Ingolia[121] using a single 250 μL aliquot of cleared lysate for each cell cycle time-point, except that cycloheximide was omitted from cultures, and frozen cells were pulverized with lysis buffer containing cycloheximide.

Sucrose gradients for fractionation were prepared as follows: all solutions were brought to RT for gradient preparation. 10% and 50% (w/v) sucrose solutions were made in 1X polysome buffer with 6 mL of each solution per gradient. Seton tubes were loaded first with 10% sucrose solution, and then under-laid with 50% solution, avoiding air bubbles. Gradients were prepared an hour before fractionation using a Biocomp Gradient Station. After running the protocol on the Gradient master, tubes were chilled at 4°C for 45 minutes.

Next, a single 250 μL aliquot of cleared lysate was used for each cell cycle time-point in biological duplicate. 300 μL of RNase I were added to each tube and tubes were incubated at 25°C for one hour. Next, 50 μL Superasein were added, samples were placed on ice and then quickly loaded onto sucrose gradients. Gradient tubes were loaded into an SW-41 Ti rotor and spun at 40,000 rpm for 2 hours at 4°C. Tubes were stored at 4°C to be processed one at a time.

Gradients were fractionated using the Piston Gradient Fractionator (Biocomp Gradient Station). Following fractionation, only eppendorf tubes containing the monosome peak were collected. Samples were acid phenol-chloroformed two times, after which RNA was ethanol precipitated in 2.5 volumes 100% EtOH, 0.3 M NaOAc and 0.5 μL LPA.

Library preparation, quality control and sequencing were performed as described above in RNA Sequencing.

Data Analysis

Data analysis was performed as in Couvillion et al.[122] Briefly, adaptor sequence was trimmed from reads and non-coding RNAs were filtered out by mapping to a collection of RNA genes downloaded from Saccharomyces Genome Database. The remaining reads were mapped allowing two mismatches to the S. cerevisiae genome assembly R64 (UCSC: sacCer3). Read counts were normalized to the total number of filtered mappers (rpm, reads per million). To determine expression values for each gene, rpm values were summed across ORFs and normalized to ORF length (RPKM, normalized reads per kilobase). For ribosome profiling reads, the first and last five codons were excluded to remove effects of translation initiation and termination. Translation efficiency (TE) was calculated by dividing ribosome profiling RPKM values by RNA-seq RPKM values. Scripts for normalization and TE calculation were written for Python 2.7.5.

Scoring Periodicity for Sequencing Data

Sequencing data were scored by the same approach described above in "Scoring Periodicity for Protein Concentration Measurements". Additionally, we filtered profiles for which the correlations between the two biological replicates had a Pearson product moment correlation coefficient below 0.5.

YMR295C CHARACTERIZATION

Spot Dilution and Liquid Culture Based Growth Assays

For spot dilution assays, saturated cultures were diluted to OD_{600} =1 in Milli-Q filtered (MQ) water in 96-well microplates and were used for subsequent 1:10 serial dilutions in MQ. The diluted cultures were used to inoculate appropriate agar plates using a sterilized pinner. For liquid-based growth assays, saturated cultures were diluted at an OD_{600} =1 in MQ water, from which 96-well microplates

containing appropriate medium were inoculated at an OD_{600} ~0.1 and growth was followed using a Sunrise™ (Tecan) microplate reader housed in an incubator for temperature control.

Split-Ubiquitin Assay

For the genomic in-frame fusion between the CRU-module and *YMR295C*, a C-terminal region of the *YMR295C* ORF was amplified (Forward primer:CCTCC CGGCCG CCGTGCCTCAGATGTCAAGAT; Reverse primer: ccacc gtcgac cc TTTCTTCTTCATTCTAC CAAA) and cloned through EagI and SalI restriction sites in front of the CRU-cassette on a pRS303 vector.[123] The plasmid was linearized in the ORF of *YMR295C* by BsgI restriction digestion and transformed into the yeast strain JD 47.[103] Site-specific integration was verified by colony PCR using diagnostic primer combinations. Large scale Split–Ubiquitin assays were performed as described.[103] A library of 383 α-strains each expressing a different Nub fusion (Table S6) were mated with the generated *YMR295C*-CRU-expressing a-strain. Diploids were transferred as independent quadruplets on SD media containing 1 mg/ml 5-FOA, and 100μM of copper sulfate to fully induce the expression of the Nub fusions. The assay was documented after three days of growth at 30°C.

Ymr295c overexpression and Aniline Blue Staining

Log phase cultures of a wild-type (BY4741) strain and a cell cycle query strain carrying an endogenous C-terminal GFP tag on *YMR295C* (genotype: *MATα can1pr::TDH3pr-E2Crimson::HPH::can1Δ::STE2pr-LEU2 CDC11-TagRFP::natMX HTA2-mCherry::kanMX YMR295C-GFP(S65T)–His3MX lyp1Δ his3Δ1 leu2Δ0 ura3Δ0 met15Δ0*), 6578, were transformed with appropriate plasmids for Gal-inducible expression of proteins of interest.[95] To construct strain 6578, a *YMR295c-GFP-HIS3* integration cassette was PCR-amplified from genomic DNA of the respective strain in the GFP-collection[23] (Forward primer: ACGCTACCAATTGTCCCTAGC; Reverse primer: TACCACTGTTGGCGGAGAG) and was used to transform a cell cycle query strain. Strains were inoculated into fresh synthetic galactose (SG) -URA media to induce either *HO* (control) or *YMR295C* overexpression. The 6578 strain was used for monitoring Ymr295c-GFP localization, and wild-type for Aniline Blue staining. After 6-9 h, 300 μl culture were spun down and cells were resuspended in LF + Methionine medium for imaging Ymr295c-GFP using an Opera Phenix (Perkin Elmer) confocal microscope and a 63x (water immersion, NA=1.15) objective (excitation 488 nm, emission 500-550 nm). For Aniline blue analysis, ≈ 0.2 OD_{600} cells were spun down at 4000 rpm for 2 min, washed with 1 ml PBS, 100 μl of 0.0025% aniline blue were added, and cells were imaged using the same microscope (excitation 405 nm, emission 435-480 nm).

Non-dataset-specific information

Human-yeast Orthologs

A list of human-yeast orthologs was retrieved from the Alliance of Genome Resources (www.alliancegenome.org/).

Functional Enrichments Analyses

Enrichment analyses for biological processes were done using the R package "fedup" (v1.10.0), available on Bioconductor (www.bioconductor.org/packages/release/bioc/html/fedup.html), and the GO Term Finder feature of the *Saccharomyces* Genome Database[124] (SGD, https://www.yeastgenome.org). Unless indicated otherwise, a cut-off of FDR-adjusted p-value ≤0.05 was used to call significance.

Multifunctionality and enrichment for GIs

All tested genes were partitioned into those that changed either localization, concentration or both localization and concentration. We tested the association of those groups with genetic interaction (GI) degree and multi-functionality as defined by the gene ontology (GO). To compare gene localization and concentration with GI degree, we used per-gene negative and positive GI degree from Costanzo et al.[88] This included data for both 786 essential and 3827 non-essential yeast genes, and in total 2878 genes overlapped with the genes studied here. Using per-gene degree, we performed Wilcoxon rank-sum testing comparing genes changing localization, concentration or both localization and concentration against the respective outgroup gene set. To assess the multi-functionality of genes changing their localization and concentration, we updated the multi-functionality index as used in Costanzo et al.[88] using the recent GO BP annotation. This provided an annotation for 3780 genes tested in this study. We performed Wilcoxon rank-sum testing comparing genes changing localization, concentration or both localization and concentration against the respective outgroup gene set. The p-values resulting from Wilcoxon rank sum testing was complemented in each of the data set comparisons with the fold-change enrichment of mean GI degree or multi-functionality index in the test group (change in either localization, concentration or both localization and concentration) over the mean of the outgroup. SAFE analyses were performed using the "Overlay Data" function on thecellmap.org.[88]

Heatmaps

Heatmaps were plotted using Heatmapper[125] and Excel. Unless explicitly stated, for heatmaps depicting cell cycle-specific dynamics the mean value across all replicates for each protein was plotted.

QUANTIFICATION AND STATISTICAL ANALYSIS

Information on statistical analyses and software, whenever relevant, are detailed throughout the results and discussion and method details sections, and the figure legends.

CellPress
OPEN ACCESS

Supplemental figures

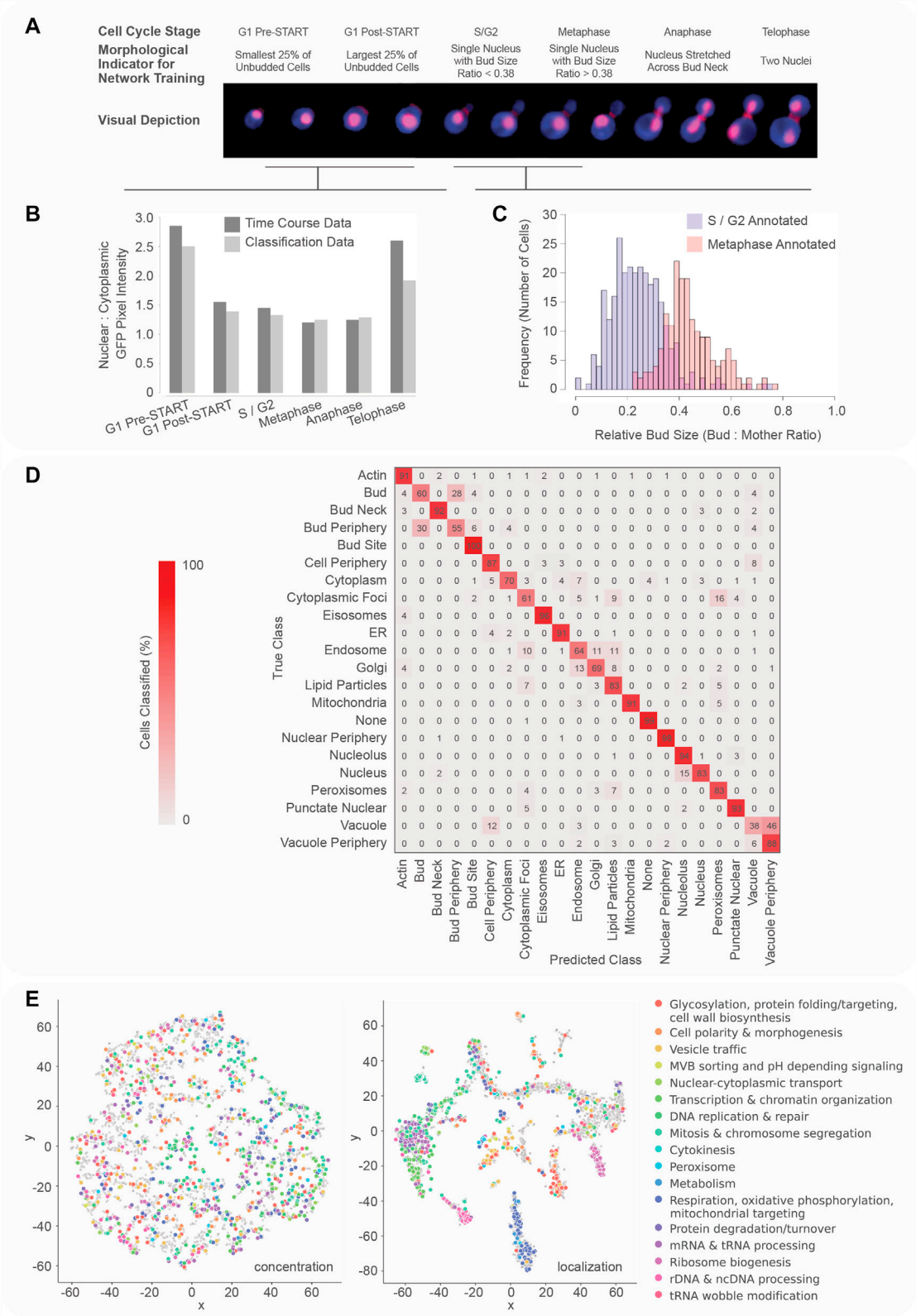

(legend on next page)

Figure S1. Automated cell cycle-stage classification and DeepLoc performance, related to Figure 1

(A) Cell cycle classification scheme used for *in silico* synchrony of images of individual cells growing in asynchronous populations. Morphological indicators used to train CycleNET are displayed along with visual representations of single-cell images corresponding to each cell cycle class.

(B) Quantification of Whi5-GFP nuclear:cytoplasmic pixel intensity for time course data versus image data that were synchronized *in silico* using our classification framework.

(C) Bud:mother size ratios for images of cells manually annotated as belonging to S/G2 or metaphase.

(D) Error matrix for the performance of DeepLoc after transfer to our dataset and additional training. Manual annotations are displayed on the y axis for 22 subcellular localizations. DeepLoc classes are displayed along the x axis, with the fraction of manually annotated cells classified into each class by DeepLoc shown on a light-to-dark red scale inside the matrix. The percentage of cells classified for each specific class comparison is shown within each cell on the matrix.

(E) t-SNE plot of cell cycle-resolved protein concentration (left) and localization (right) data for proteins measured in both (n = 3,806). Each protein is represented by a dot. Proteins are annotated based on a published functional standard.[88]

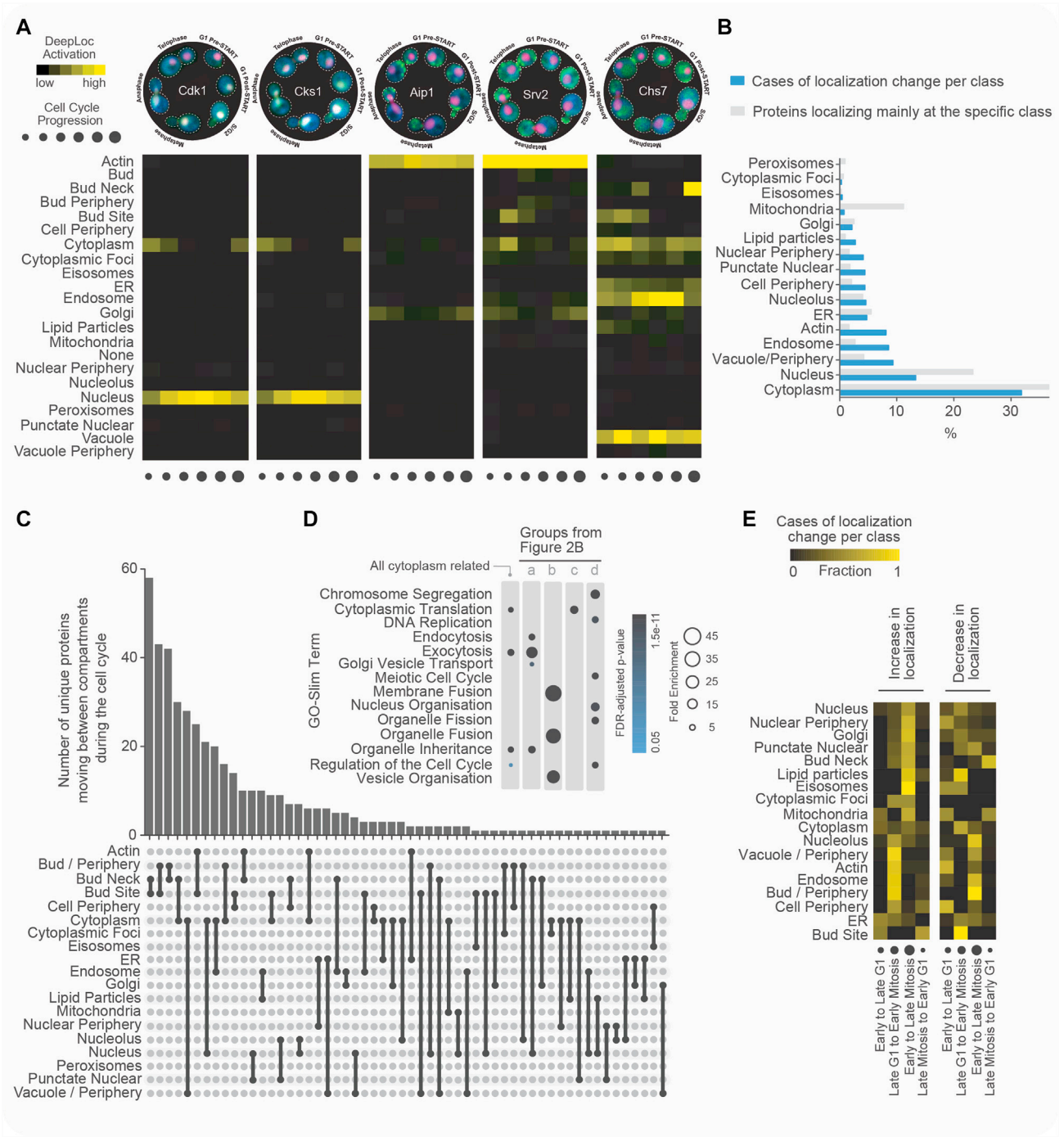

Figure S2. Examples of identified cycle-specific localization changes and localization class-connectivity, related to Figure 2

(A) Clustergram cross-section showing the average cell cycle localization vector (DeepLoc activation) on a yellow-black scale for several proteins that show distinct localization patterns through the cell cycle. Example micrographs for each protein are shown above the heatmap (cytoplasm displayed in blue, the nucleus and septin in red/pink, and the protein of interest in green).

(B) Graph illustrating the percentage of cases of localization change (n = 653) per localization class, and percentage of proteins (n = 3,329) that localize primarily at each class (determined by estimating the mean DeepLoc activation throughout the cell cycle of each protein for each class), for localization classes with presence in all cell cycle phases.

(C) Graph summarizing the number of unique proteins moving between two localization classes. The involved localizations for each case are illustrated below the graph.

(legend continued on next page)

(D) Functional enrichments (GO-Slim terms) of proteins involved in the localization class-groups outlined in Figure 2B as groups a, b, c, and d, as well as of all proteins involved in cytosol-related movements.
(E) Heatmap showing the fraction of cases of localization change per cell cycle transition for each localization class. For each localization class, the fractional changes sum to one. Increases and decreases in localizations are graphed separately.

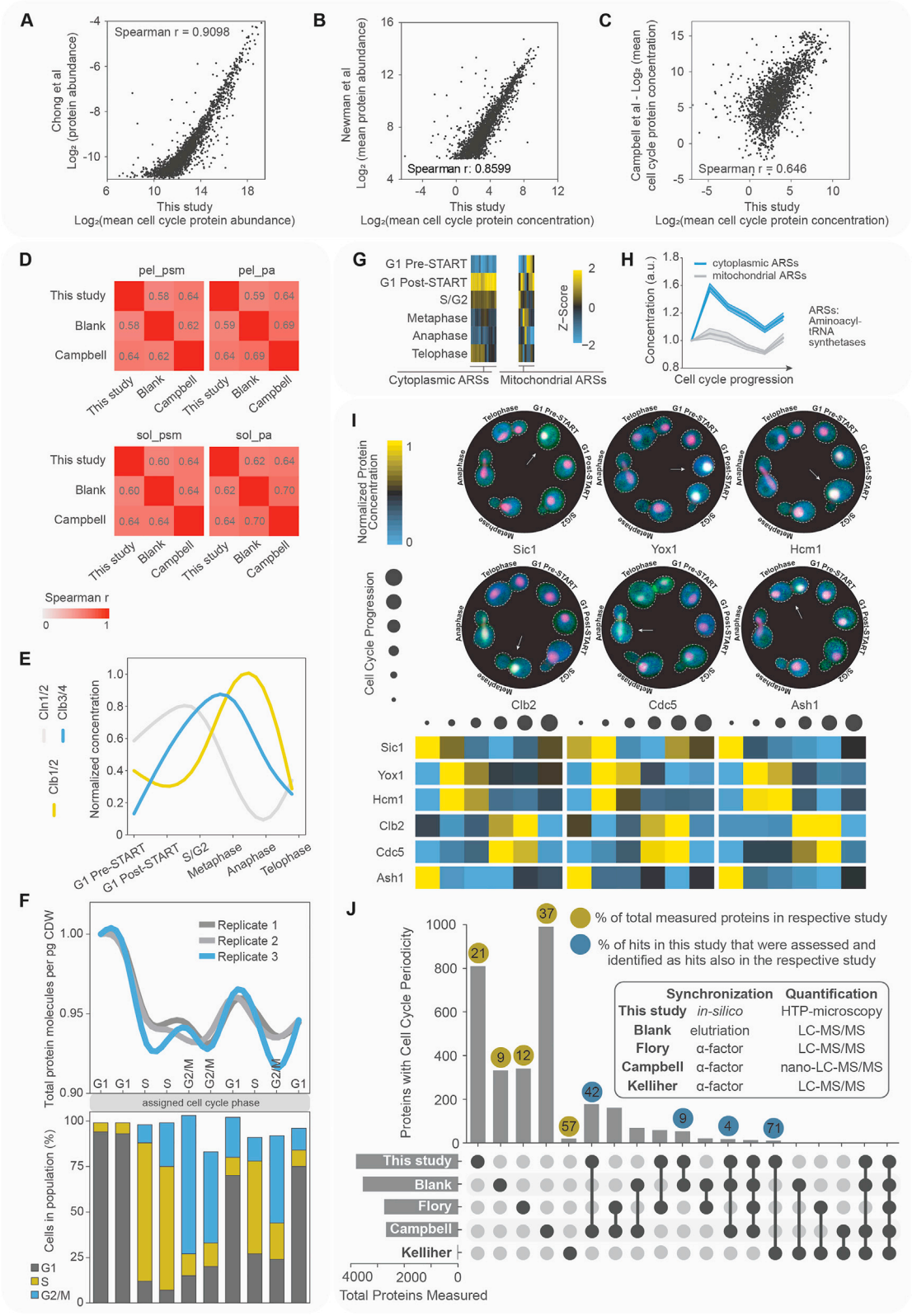

(legend on next page)

Figure S3. Quality control and cross-study comparison of cell cycle-specific proteome dynamics, related to Figure 3

(A–C) Correlation of protein abundance measurements acquired in this study with (A) microscopy-acquired[25] (n = 2,198), (B) fluorescence-activated cell sorting (FACS)-acquired[55] (n = 2,202), and (C) mass-spectrometry-acquired[18] (n = 2,022) proteome measurements.

(D) Correlation of $\log_2$-transformed, mean cell cycle levels of commonly measured proteins in this study, and the studies of Blank et al.[4] and Campbell et al.[18] (sol, soluble protein extracts; pel, insoluble pellet; psm, spectral counts; pa, peak areas, from respective datasets in Blank et al.).

(E) Smoothed (cubic spline) concentration dynamics of the indicated cyclins (mean normalized concentration across all replicates for each cyclin pair) during the cell cycle. Note that due to degradation and periodic expression,[126–128] cyclin levels may fall below detection limit at certain cell cycle phases. The complete trajectories were used.

(F) Graph of protein molecules per cell dry weight (CDW) during the cell cycle. The corresponding distributions of cells in each cell cycle phase are shown in the bar graph. Data were taken from Campbell et al.[18]

(G) Heatmap showing the concentration dynamics of cytoplasmic (n = 13) and mitochondrial (n = 8) aminoacyl-tRNA synthetases (ARSs), relative to G1 pre-START (mean ± SEM). The ARS Grs2 that is not produced under normal conditions is not shown.

(H) Graph showing the concentration of proteins in (G), relative to G1 Pre-START (mean ± SEM).

(I) Examples of proteins that are known to display cell cycle-specific concentration that were also identified as periodic in this study. Example micrographs (above; cytoplasm displayed in blue, the nucleus and septin in red/pink, and the protein of interest in green) and normalized protein concentrations at each replicate (below) are shown. Complete cell cycle trajectories were used for the estimation of normalized levels even for proteins with below detection-limit levels at specific cell cycle phases.

(J) Summary of overlap between proteins identified as periodic in concentration during the cell cycle in our study and in previous studies.[4,18,20,129] The synchronization and quantification methods are indicated in the inset. Percentage agreement among studies (indicated inside the blue circles) is defined as the fraction of common hits identified in these studies, divided by the set of common proteins that were assessed for periodicity in these studies.

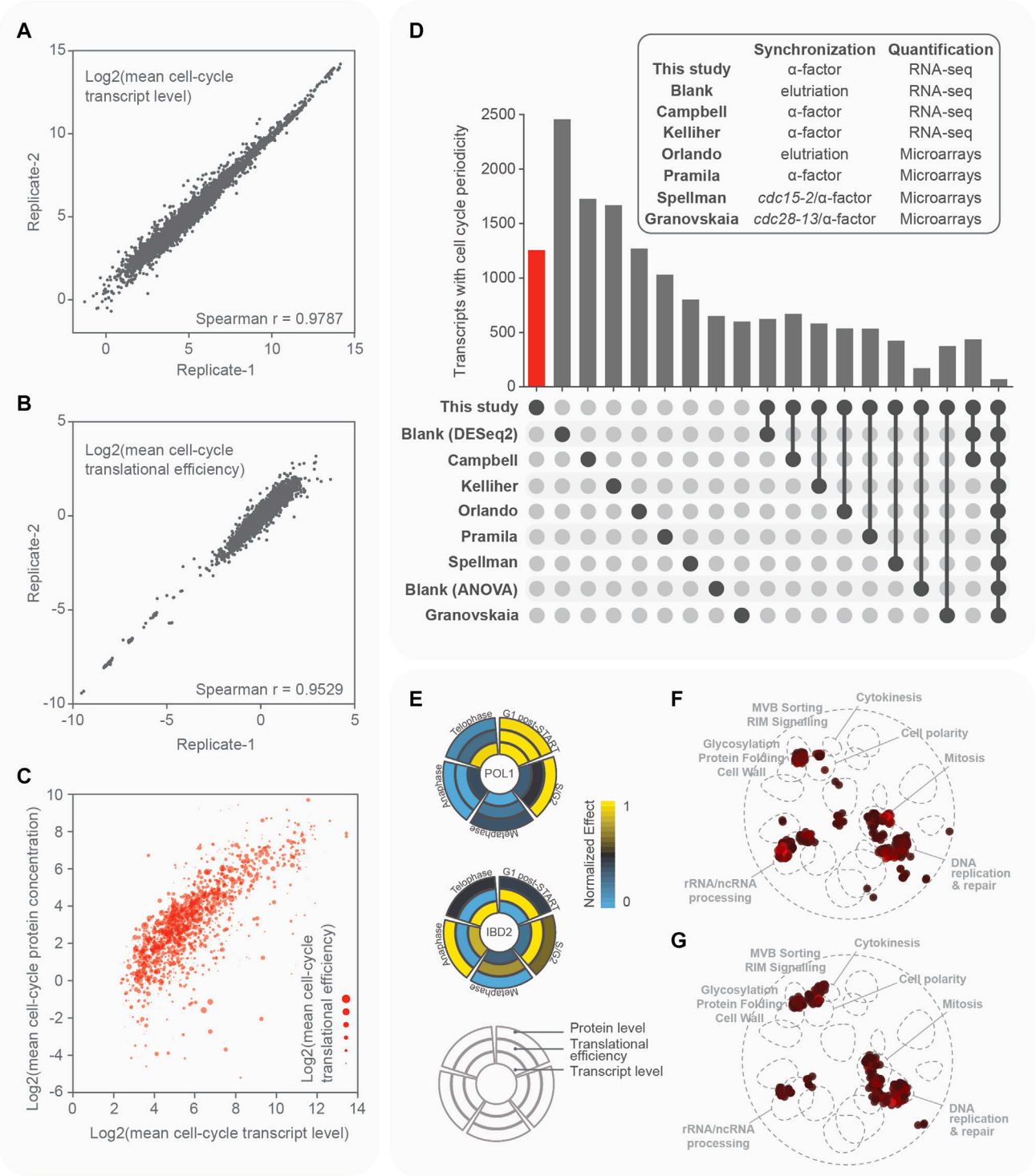

Figure S4. Quality control and cross-study comparison of cell cycle-specific gene expression data, related to Figure 4

(A and B) Comparison between biological replicates for (A) transcript level (n = 5,549) and (B) translational efficiency (n = 4,766) measurements.

(C) Correlation between transcript level, translational efficiency, and protein concentration measurements for each gene (n = 3,307; Spearman r: 0.746, 0.3377, and 0.2932, for transcript level and protein concentration, translational efficiency and protein concentration, and transcript level and translational efficiency, respectively; in all cases, two-tailed p value < 0.0001). The mean value between all biological replicates in each dataset was used for each gene.

(D) Comparison of overlap between transcripts identified to display periodic level during the cell cycle among the current and previous studies.[4,7,12,18,74,79,80]

(legend continued on next page)

(E) Cell cycle-specific profiles showing normalized transcript level, translational efficiency, and protein concentration dynamics for *POL1* and *IBD2*. While Pol1 did not pass our criteria for periodicity in protein concentration, we could still detect the small cell cycle-related changes of its dynamics as previously reported.[130] *IBD2* transcript levels were not significantly periodic.

(F) Spatial analysis of functional enrichment (SAFE) analysis of all genes identified recently as cell cycle-dependent in human cells[22] that also have yeast orthologs, which were measured in this study (n = 133 human genes and 157 yeast orthologs). Functional enrichments associated with the gene set are visualized within an outline of the global similarity network of yeast genetic interactions visualized using SAFE, which identifies regions of the network enriched for specific biological processes.[88] Regions of the network corresponding to relevant bioprocesses are labeled.

(G) SAFE map for the fraction of genes in (F) that were also identified in this study to be periodic in at least protein concentration or localization (n = 45 human genes and 46 yeast orthologs).

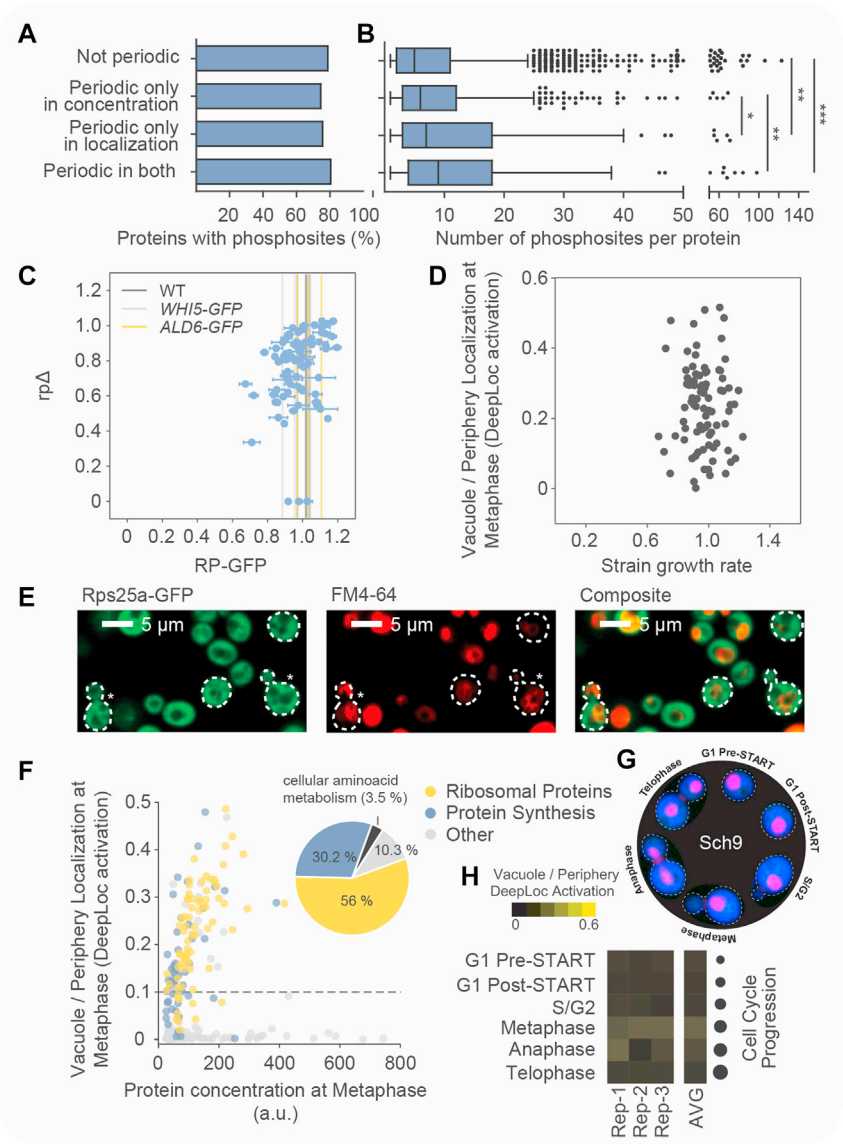

Figure S5. Spatiotemporal analysis of the cell cycle-periodic proteome, related to Figure 5

(A) Percentage of proteins in the sets indicated on the left of the bar graph with known phosphosites (not periodic, n = 2,732; periodic only in concentration, n = 677; periodic only in localization, n = 272; periodic in both, n = 133).

(B) Number of phosphosites per protein among proteins with known phosphosites in each set (unpaired t test with Welch's correction in ranked data,[131] *p value = 0.0155; **p value = 0.0030 (periodic only in concentration versus periodic in both); **p value = 0.0017 (not periodic versus periodic only in localization); ***p value = 0.0010).

(C) Growth rate comparison between RP-GFP fusions strains (mean ± SEM from three technical replicates) and respective single mutant fitness as previously reported.[132] Each dot represents a different protein (n = 85), and vertical lines the growth rates of WT and other control GFP-fusion strains (Ald6-GFP, Whi5-GFP). Mutant fitness for essential RP genes is set to zero.

(D) Mean growth rate of respective RP-GFP strains from (C) normalized to the mean of all controls versus predicted localization of the protein at the vacuole and/or its periphery during metaphase.

(E) Microscopy images of Rps25a-GFP cells stained with the vacuolar marker FM 4-64. Two late G1 and two mitotic (denoted by asterisk) cells are highlighted. A composite of the images is also shown.

(F) Protein concentration versus predicted localization at the vacuole and/or its periphery during metaphase of the most abundant (top 25%) proteins in our study (n = 251) (mostly cytoplasmic localization, DeepLoc activation ≥ 0.5) Inset: pie chart showing the fraction of proteins with DeepLoc activation ≥ 0.1 (vertical dotted line) belonging to each indicated functional group. Group "protein synthesis" includes proteins involved in protein synthesis, other than ribosomal proteins.

(G and H) (G) Sch9 example micrographs (cytoplasm displayed in blue, the nucleus and septin in red/pink, and the protein of interest in green) and (H) corresponding heatmaps of DeepLoc activation involving the class vacuole/periphery.

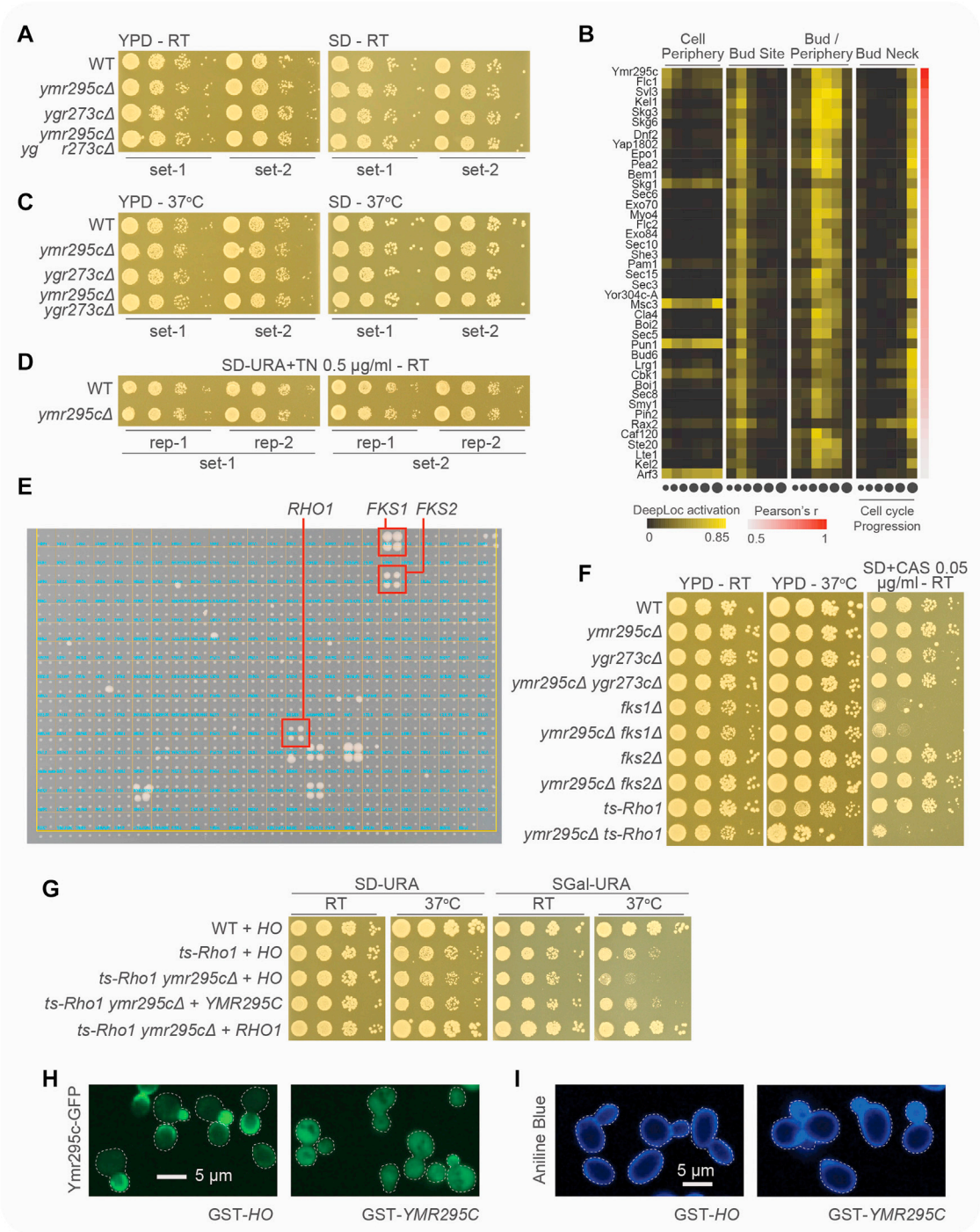

Figure S6. Cell cycle-resolved phenomics for functional analysis and exploration of new biology, related to Figure 6

(A) Spot dilution assays on YPD (left) and SD (right) media for the indicated strains grown at room temperature (RT). Set-1 and Set-2 denote spots of strains from different precultures.

(B) Heatmap of DeepLoc activation associated with indicated localization class (top of heatmap) showing cell cycle-specific changes in protein localization of proteins with similar (Pearson's r $\geq$ 0.5) localization profiles to Ymr295c, ordered by degree of similarity. Localization dynamics for four relevant classes are shown.

(C) Same as (A), but plates were incubated at 37°C.

(D) Spot dilution assays for WT and *ymr295CΔ* strains grown in the presence of tunicamycin (TN). Rep-1 and Rep-2 denote different technical replicates.

(legend continued on next page)

(E) Split-Ub interaction assay of 383 yeast strains co-expressing P_{MET17}-*YMR295C*- C_{ub}-RUra3 each with a different N_{ub} fusion protein. Four independent matings were spotted as quadruplet on SD medium containing 5-FOA and 100 μM copper sulfate. Shown is the growth of the diploid yeast cells after 3 days at 30°C. Growth indicates a protein-protein interaction. Highlighted in blue is the matrix revealing the identities of the respective Nub-fusions. Boxed are the quadruplets indicating a specific Split-Ub-based interaction. Growth was observed for Fks1, Fks2, Rho1, Snc1, and Sso1, as well as the technical false-positives Cpn6 and Bnr1.
(F) Spot dilution assays of a WT strain and the indicated single and double mutants grown in the indicated conditions (RT, room temperature; CAS, caspofungin).
(G) Complementation spot dilution assays of strains expressing *HO*, *YMR295C*, or *RHO1*, via a MoBY plasmid,[94] grown in the indicated conditions.
(H and I) (H) Microscopy images of Ymr295c-GFP and (I) aniline blue-stained WT cells in which either *HO* or *YMR295C* is overexpressed via a Gal-induced plasmid[95] in synthetic galactose (SG)-URA. Aniline blue is a specific stain for 1,3-beta-glucan.[133]